Bifurcation analysis of cantilever beams in channel flow

Filipe Soares, Christophe Vergez, Jose Antunes, Bruno Cochelin, Vincent Debut, Fabrice Silva

Journal of Sound and Vibration 567 (2023) 117951

Contents lists available at ScienceDirect

Journal of Sound and Vibration

journal homepage: www.elsevier.com/locate/jsvi

Bifurcation analysis of cantilever beams in channel flow

Filipe Soares [a,*], Christophe Vergez [c], Jose Antunes [a], Bruno Cochelin [c], Vincent Debut [a,b], Fabrice Silva [c]

[a] Instituto Superior Técnico – C2TN, Laboratory of Applied Dynamics, Lisbon, Portugal
[b] Instituto Politécnico de Castelo Branco – ESAA, Castelo Branco, Portugal
[c] Aix-Marseille Université, CNRS, Centrale Marseille, LMA UMR7031, Marseille, France

ARTICLE INFO

Keywords:
Flow-induced vibration
Flutter
Beam in axial flow
Bifurcation analysis
Hysteresis
Sub-critical bifurcation
Quasi-periodic oscillations

ABSTRACT

The flutter of cantilevered beams in channel flow is a benchmark example of flow-induced vibrations and its fundamental behaviour is found in numerous practical applications. Experiments have shown that such systems present a wide variety of complex nonlinear behaviour. However, the plethora of previous studies is mostly concerned with linear stability analysis. In this work, we provide an initial impulse for a comprehensive nonlinear study of these systems through bifurcation analysis. We consider a one-dimensional problem, where a cantilevered beam is treated in a modal framework and the surrounding flow is modelled by bulk-flow equations. The system is discretized in space and time via Galerkin procedures (modal, Tau and harmonic balance) and the continuation of periodic solutions is achieved using the asymptotic numerical method. Additionally, a numerical method for an "augmented" linear stability analysis is proposed, allowing the continuation of Hopf bifurcation branches, including their sub- or super-critical nature. The nonlinear dynamics are explored with respect to various dimensionless parameters. Results illustrate a number of behavioural trends: sub-critical bifurcations and hysteresis loops, internal resonances, grazing boundaries (separation between limit cycles with and without intermittent beam-wall impacts) as well as torus bifurcations and quasi-periodic oscillations.

1. Introduction

A flexible cantilevered plate subject to uniform axial flow may lose stability at sufficiently large flow velocities, as is seen in the familiar example of a flag flapping in the wind. This type of fluid-structure interaction (FSI) systems has become a canonical example of flow-induced vibrations [1] as its fundamental behaviour can be found in various practical contexts: energy harvesting devices [2], paper and aeronautic industry [3,4], wind musical instruments [5] and even human snoring [6]. Experimental observations have shown that, despite its apparent simplicity, these FSI systems can undergo rather complex dynamical behaviour. In addition to the well-documented fluttering (periodic) motions, experiments have also shown large hysteresis loops (generally attributed to sub-critical bifurcations) quasi-periodic motions and even chaotic dynamics at specific flow velocity ranges [7–9].

Despite the large body of literature published on the subject over the last decades, many important aspects of the underlying physics are still not well understood. For example, we underline the fact that models often underestimate critical velocities, particularly for relatively heavy beams. Another poorly understood phenomenon is the commonly observed hysteresis loops, i.e. when gradually

* Corresponding author.
E-mail address: filipe.soares@ctn.tecnico.ulisboa.pt (F. Soares).

https://doi.org/10.1016/j.jsv.2023.117951
Received 26 May 2023; Received in revised form 1 July 2023; Accepted 16 July 2023
Available online 18 July 2023

increasing the flow velocity, an initially static plate will start to oscillate at a particular critical point U_1, while when decreasing flow velocity, an initially fluttering plate will stop oscillating at a lower critical point $U_2 < U_1$. This suggests the existence of bi-stable regions which is typically associated to sub-critical bifurcations. However, with few exceptions, most developed models predict super-critical bifurcations (no hysteresis) [10]. Finally, the occurrence of quasi-periodic solutions and the routes to chaos are still not well understood.

A wide variety of theoretical models and numerical methods have been used to study the dynamics of the fundamental problem, in both open-flow and channel-flow configurations [11]. While the plate is generally modelled as a beam, including or not nonlinear geometric effects, the flow modelling presents much more diversity: different variants of potential flow models (some including lumped vortex models), leakage-flow approaches and incompressible Navier-Stokes equations in 2-D and 3-D domains are commonly found in literature [10,12-14]. However, by and large, the plethora of models developed so far deal mostly with the critical stability conditions, typically (but not always) using linearized equations of motion [15–17]. Knowledge of the conditions for instability and how they are affected by the various parameters of the system is crucial for the understanding of the FSI dynamics. However, they provide little insight into the ensuing nonlinear motions, which may be valuable for various practical applications. For example, the fact that linearized systems (by default) ignore hysteretic behaviour, means they will predict stable equilibria when oscillating states may co-exist. Naturally, such simplifications can have disastrous effects in applications where oscillating behaviour needs to be avoided.

Nevertheless, some recent studies have considered nonlinear models of beams in axial flow, both in channel-flow (confined) and open-flow configurations, in order to calculate the limit-cycles oscillations (LCO) stemming from a linearly unstable system. In the context of open-flow configurations, we underline the work of Tang & Paidoussis [10] who considered a lumped vortex model to calculate the pressure difference across a 2-D inextensible beam. Overall, their modelling results compared qualitatively well with experiments, even though subcritical bifurcations and hysteresis loops were not observed. Using a similar model, Chen et al. [9] managed to recreate the quasi-periodic dynamics observed in experiments, and suggested the "route to chaos" is caused by torus bifurcations. A few nonlinear models have also been developed for confined configurations using both direct methods to solve the Navier-Stokes equation in 2-D [18] as well as more compact one-dimensional leakage-flow approaches [19]. In the case of channel flow however, impacts of the beam against the channel walls is a predominant behaviour which presents additional difficulties to the nonlinear modelling [20,21]. Hence, these studies are generally limited to relatively narrow regions of the parameter space. Nevertheless, in a recent work [22], the authors have considered a pragmatic impact model and presented several illustrative results of limit-cycles including intermittent impacts.

In a few studies, models showing hysteretic/sub-critical behaviour have also been proposed. In [23], Eloy et al. proposed a weakly nonlinear flow model using the unsteady Bernoulli equation truncating nonlinear terms up to cubic order. In [24], Alben & Shelley considered a 2-D inviscid flow, including the vortex sheet formed downstream. In both studies, numerical results showed both super-critical and sub-critical bifurcations, depending on specific parameter configurations, even though the width of the calculated hysteresis loops $\eta = (U_1 - U_2)/U_1$, is considerably smaller (1–10%) than the values observed experimentally (20–60%).

Past studies, either experimental or theoretical, have already shed light on the diversity of nonlinear dynamics found in these systems. However, a comprehensive nonlinear analysis is often difficult to attain, as most numerical methods/models are very costly and typically rely on temporal integrations of the equations of motion. These give us a local perspective of the system dynamics and are less practical for broader parametric studies. This fact is worth underlying because, even in the simplest symmetric case, system dynamics have been shown to depend greatly on a set of dimensionless parameters: the beam-to-fluid mass ratio, the reduced velocity, Reynolds number, plate aspect ratio, structural damping and confinement ratio (channel height to beam length) [15].

In this work, we aim to provide an initial impulse for a comprehensive nonlinear study in these types of systems through bifurcation analysis [25]. We consider a one-dimensional problem, where a cantilevered beam is treated in a modal framework and the surrounding flow is modelled by bulk-flow equations. In essence, assuming the solutions of the coupled problem are periodic, the equations of motion can be discretized in time using the harmonic balance method [26], leading to a nonlinear algebraic system. Then, branches of periodic solutions can be calculated with respect to one, or multiple, control parameters [27]. These continuation approaches are not only more computationally efficient, but they also provide a more complete overview of the system dynamics, allowing for example, the differentiation between super/sub-critical bifurcations, the detection of period-doubling or torus bifurcations, internal resonances, etc. [28].

The physical model is described in Section 2, while the discretization and continuation procedures are described in Sections 3 and

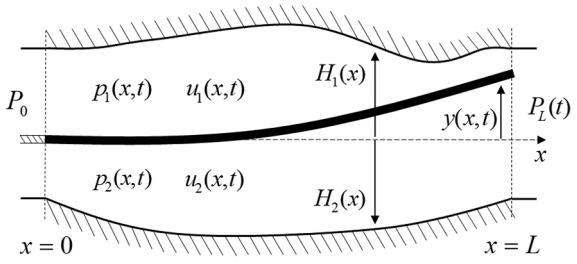

Fig. 1. Diagram of the 1D model.

4. In Section 5, the question of hysteresis and sub-critical bifurcations are discussed in light of the extensive parametric studies performed. Finally, the rich variety of nonlinear dynamics encountered is illustrated and discussed in Section 6.

2. Model description

The considered model describes the FSI of a flexible beam in channel flow as shown in Fig. 1. The present formulation is generic with regards to beam boundary conditions, variations in the channel cross-section as well as flow direction. However, here we focus on the particular case of cantilevered beams subject to axial flow in the positive $x-$ direction, in channels of constant height. In this section, all variables are presented in dimensionless form with respect to the beam's length L, total mass $m_0 = \rho_s AL$, and a characteristic frequency

$$\omega_0 = \frac{\sqrt{EI/\rho_s A}}{L^2} 2\pi \tag{1}$$

where ρ_s, A and EI are the density, cross-sectional area and bending stiffness of the beam, respectively.

2.1. Structure dynamics

The dynamics of a linear cantilevered beam are defined in a modal framework, i.e. in terms of a finite number M of *in-vacuo* beam modes. The vertical displacement of the beam $y(x,t)$ is developed as

$$y(x,t) = \sum_{m=1}^{M} \varphi_m(x) q_m(t) \tag{2}$$

where $q_m(t)$ and $\phi_m(x)$ are the dimensionless modal displacements and shapes, respectively. The dynamics of the beam are given, as usual, by the modal equations

$$m_m \ddot{q}_m(t) + 2m_m \omega_m \zeta_m \dot{q}_m(t) + m_m \omega_m^2 q_m(t) = F_m(t), \quad m = 1,\ 2\ \ldots\ M \tag{3}$$

where m_m, ω_m, ζ_m and $F_m(t)$ are the masses, frequencies, damping ratios and external forces associated with each beam mode m. The external modal forces $F_m(t)$ are then given by the projection of the flow pressure fields on the upper and lower sides of the beam, $p_1(x,t)$ and $p_2(x,t)$, unto the modal basis

$$F_m(t) = M^* \int_0^1 [p_2(x,t) - p_1(x,t)]\, \varphi_m(x) dx, \quad m = 1,\ 2\ \ldots M \tag{4}$$

where the fluid-beam mass ratio is written explicitly as $M^* = \rho L / \rho_s e$, ρ being the density of the fluid and e denotes the thickness of the beam.

2.2. Fluid dynamics

In the context of bulk-flow theory [29,30], channel heights are considered to be relatively small compared to the characteristic length L. Consequently, variations in flow pressure $p_c(x,y,z,t)$ and velocity $u_c(x,y,z,t)$ along their cross-section are considered negligible, and hence, these are taken as the cross-sectionally averaged, $p_c(x,t)$ and $u_c(x,t)$. The variable channel heights $h_c(x,t)$ are defined in terms of the beam motion and the channel profiles

$$\begin{cases} h_1(x,t) = H_1(x) - \sum_{m=1}^{M} \varphi_m(x) q_m(t) \\ h_2(x,t) = H_2(x) + \sum_{m=1}^{M} \varphi_m(x) q_m(t) \end{cases} \tag{5}$$

where $H_1(x)$ and $H_2(x)$ are the distances from the upper and lower walls to the beam equilibrium position, respectively, and the index c denotes the upper $(c=1)$ or lower $(c=2)$ channels. Assuming incompressible flow, the momentum and continuity equations for the flow in each channel c are given in dimensionless form by

$$\frac{\partial u_c}{\partial t} + u_c \frac{\partial u_c}{\partial x} + \frac{\partial p_c}{\partial x} + \frac{u_c^2 f}{h_c} = 0 \tag{6}$$

$$\frac{\partial h_c}{\partial t} + \frac{\partial}{\partial x}(h_c u_c) = 0 \tag{7}$$

where f is a Fanning friction coefficient. The dissipative term in the momentum equation $u_c^2 f / h_c$ describes the distributed head-losses which encapsulate in a simplified manner viscous, turbulent or boundary layer effects. Formally, this term should actually be written as

$u_c|u_c|f$, to account for the possibility of reverse flow, which might occur locally at large amplitude beam motions. However, for simplicity of the formulation, we use its quadratic simplification $u_c^2 f$ based on the argument that scenarios with reverse flow are rare and generally very brief and locally concentrated, and hence, unlikely to affect the dynamics significantly. Neglecting this frictional term, the momentum equation reduces to its commonly used inviscid form

$$\frac{\partial u_c}{\partial t} + u_c \frac{\partial u_c}{\partial x} + \frac{\partial p_c}{\partial x} = 0 \tag{8}$$

Additionally, localized dissipative effects are enforced at the boundary conditions which aim to encapsulate, in a compact manner, the energy losses occurring outside the domain. The complex phenomena associated with these energy losses is diverse and can vary significantly with local geometry (e.g. area constriction/expansion) and flow conditions. However, a common approach is to use a quasi-steady Bernoulli relation that includes head-loss terms, whose coefficients are typically taken from empirical data [31]. Following previous works [12,16], the second order system Eq. (7)-(8) is then submitted to the following boundary conditions at $x = 0$ and $x = 1$:

$$\begin{aligned} p_c(0,t) &= P_0(t) - \frac{1}{2}[u_c(0,t)]^2 - \frac{1}{2}|u_c(0,t)|u_c(0,t)K_0 \\ p_c(1,t) &= P_L(t) - \frac{1}{2}[u_c(1,t)]^2 + \frac{1}{2}|u_c(1,t)|u_c(1,t)K_L \end{aligned} \tag{9}$$

where K_0 and K_L are the entry and exit head-loss coefficients, while $P_0(t)$ and $P_L(t)$ represent pressures imposed at distant reference chambers (where flow velocity is zero) located upstream and downstream of the domain, respectively. For configurations with a cantilevered beam, the head-loss coefficient K_0 will not have a significant effect on the dynamics, as it acts on the clamped end of the structure. For steady flow in the positive direction, it acts simply as a control-valve, effectively limiting the flow entering the domain. On the other hand, the expected vortical effects at the trailing-edge suggest that K_L will have a significant effect on the coupling dynamics. For such configurations, several studies have shown that setting $K_0 = 0$ and $K_L = 1$ yields satisfactory results, as predicted stability boundaries compare reasonably well with results from 2-D models [22,16] as well as experiments [12].

3. Galerkin formulation

In this section we present only a brief summary of the used Galerkin formulation, which serves to discretize the system of partial differential equations Eq. (7)-(8) into a set of time-dependant (ordinary differential and algebraic) equations. The interested reader is referred the authors previous work for more details [32]. For simplicity of illustration, we showcase the formulation for the inviscid case, i.e. using the momentum Eq.(8), while noting that the same procedure can be applied using Eq.(6). In essence, the flow pressure and velocity fields, $u_c(x,t)$ and $p_c(x,t)$, are developed in terms of a series of Chebyshev polynomials of the first-kind. These form a complete basis of orthogonal functions which are suited to describe flow fields with simple linear changes as well as fields of any complexity. Because we need to project the Chebyshev basis in our domain interval $x = [0,\ 1]$, we use a shifted Chebyshev basis, defined by the recursive relation

$$T_0(x) = 1 \ ; \ \ T_1(x) = 2x - 1 \ ; \ \ T_n(x) = 2(2x-1)T_{n-1}(x) - T_{n-2}(x) \tag{10}$$

where the associated shifted orthogonality kernel is given by

$$w(x) = \frac{1}{\sqrt{1-(2x-1)^2}} \tag{11}$$

Then, the velocity and pressure fields, $u_c(x,t)$ and $p_c(x,t)$, truncated to $N+1$ polynomials, are given by

$$u_c(x,t) = \sum_{n=0}^{N} T_n(x)u_n(t) \quad ; \quad p_c(x,t) = \sum_{r=0}^{N} T_r(x)p_r(t) \tag{12}$$

where the generic velocity expansion coefficients $u_n(t)$ are replaced by $\widehat{u}_n(t)$ or $\breve{u}_n(t)$ when referring to the lower or upper channels, respectively. A similar notation is taken for the pressure coefficients.

Replacing the expansions in (12) into the momentum (8) and continuity (7) equations as well as in the boundary conditions (9), and proceeding with a classical Galerkin projection would lead to an over-determined system. That is, for each channel c we would have $2(N+1)$ variables $(\breve{u}_n,\ \breve{p}_r)$ and $2(N+1)+2$ equations (that is: $N+1$ momentum equations, $N+1$ continuity equations and two boundary conditions). Hence, the so-called Tau-method [33] is used here, where the Galerkin projection is made unto a reduced basis of N polynomials instead. This allows us to account for the nonlinear, time-dependant boundary conditions in a well-posed manner.

After the Tau-Galerkin projection on the fluid equations of each channel $c = 1,2$, and assembly with the structural equations (3) in state-space form, with $r_m(t) = \dot{q}_m(t)$, the final coupled system is written in matrix form as

$$\begin{bmatrix} [\mathbf{I}] & 0 & 0 & 0 & 0 & \cdots & 0 \\ 0 & [\mathbf{I}] & 0 & 0 & 0 & & \\ 0 & 0 & [\mathbf{E}] & 0 & 0 & & \\ 0 & 0 & 0 & [\mathbf{E}] & 0 & & \\ 0 & 0 & 0 & 0 & 0 & & \\ \vdots & & & & & \ddots & \\ 0 & & & & & & 0 \end{bmatrix} \begin{Bmatrix} \dot{\mathbf{R}} \\ \dot{\mathbf{Q}} \\ \breve{\dot{\mathbf{U}}} \\ \hat{\dot{\mathbf{U}}} \\ \breve{\dot{\mathbf{P}}} \\ \hat{\dot{\mathbf{P}}} \end{Bmatrix} + \begin{bmatrix} [\mathbf{Z}] & [\Omega] & 0 & 0 & [\mathbf{S}] & -[\mathbf{S}] \\ -[\mathbf{I}] & 0 & 0 & 0 & 0 & 0 \\ 0 & 0 & 0 & 0 & [\mathbf{D}] & 0 \\ 0 & 0 & 0 & 0 & 0 & [\mathbf{D}] \\ -[\mathbf{A}] & 0 & [\mathbf{B}] & 0 & 0 & 0 \\ [\mathbf{A}] & 0 & 0 & [\mathbf{C}] & 0 & 0 \\ 0 & 0 & 0 & 0 & \mathbf{T}_0 & 0 \\ 0 & 0 & 0 & 0 & 0 & \mathbf{T}_0 \\ 0 & 0 & 0 & 0 & \mathbf{T}_L & 0 \\ 0 & 0 & 0 & 0 & 0 & \mathbf{T}_L \end{bmatrix} \begin{Bmatrix} \mathbf{R} \\ \mathbf{Q} \\ \breve{\mathbf{U}} \\ \hat{\mathbf{U}} \\ \breve{\mathbf{P}} \\ \hat{\mathbf{P}} \end{Bmatrix} = \begin{Bmatrix} \mathbf{0} \\ \mathbf{0} \\ -\breve{\mathbf{F}}_r \\ -\hat{\mathbf{F}}_r \\ \breve{\mathbf{H}}_n \\ -\hat{\mathbf{H}}_n \\ \breve{V}_0 \\ \hat{V}_0 \\ \breve{V}_L \\ \hat{V}_L \end{Bmatrix} \tag{13}$$

where $[\mathbf{I}]$ is the identity matrix; $[\Omega] = \mathrm{diag}(\omega_m^2)$ and $[\mathbf{Z}] = \mathrm{diag}(2\zeta_m\omega_m)$ are the diagonal stiffness and damping matrix of the beam. The spatial operator matrices $[\mathbf{A}] - [\mathbf{E}]$ and $[\mathbf{S}]$ are given by

$$\begin{aligned}
[\mathbf{A}] &= A_{mn} = \int_0^1 \varphi_m(x) T_n(x) dx, && \begin{cases} m = 1, 2, \cdots, M \\ n = 0, 1, \cdots, N-1 \end{cases} \\
[\mathbf{B}] &= B_{sn} = \int_0^1 \left[H'_1(x) T_s(x) + H_1(x) T'_s(x) \right] T_n(x) dx, && \begin{cases} s = 0, 1, \cdots, N \\ n = 0, 1, \cdots, N-1 \end{cases} \\
[\mathbf{C}] &= C_{sn} = \int_0^1 \left[H'_2(x) T_s(x) + H_2(x) T'_s(x) \right] T_n(x) dx, && \begin{cases} s = 0, 1, \cdots, N \\ n = 0, 1, \cdots, N-1 \end{cases} \\
[\mathbf{D}] &= D_{sr} = \int_0^1 T'_s(x) T_r(x) w(x) dx, && \begin{cases} s = 0, 1, \cdots, N \\ r = 0, 1, \cdots, N-1 \end{cases} \\
[\mathbf{E}] &= E_{sr} = \int_0^1 T_s(x) T_r(x) w(x) dx, && \begin{cases} s = 0, 1, \cdots, N \\ r = 0, 1, \cdots, N-1 \end{cases} \\
[\mathbf{S}] &= S_{mr} = \frac{M^*}{m_m} \int_0^1 T_r(x) \varphi_m(x) dx, && \begin{cases} m = 1, \cdots, M \\ r = 0, 1, \cdots, N \end{cases}
\end{aligned} \tag{14}$$

while the nonlinear vectors $\mathbf{F}_r$ and $\mathbf{H}_n$ on the right-hand-side are given by

$$\begin{aligned}
\mathbf{F}_r &= \sum_{n=0}^{N} \sum_{s=0}^{N} \left[\int_0^1 T'_n(x) T_s(x) T_r(x) w(x) dx \right] u_n(t) u_s(t) \\
\mathbf{H}_n &= \sum_{m=1}^{M} \sum_{s=0}^{N} \left[\int_0^1 \left[\varphi'_m(x) T_s(x) + \varphi_m(x) T'_s(x) \right] T_n(x) dx \right] q_m(t) u_s(t)
\end{aligned} \tag{15}$$

where replacing the generic coefficients $u_n(t)$ by the coefficients for a particular channel, $\breve{u}_n(t)$ or $\hat{u}_n(t)$, will yield the corresponding vectors $\breve{\mathbf{F}}_r$ and $\breve{\mathbf{H}}_n$ or $\hat{\mathbf{F}}_r$ and $\hat{\mathbf{H}}_n$, respectively. Finally, the discretized boundary conditions are defined by the vectors $\mathbf{T}_0 = T_r(0)$ and $\mathbf{T}_L = T_r(1)$, as well as the nonlinear terms on the right-hand-side

$$\begin{aligned}
V_0 &= P_0(t) - \frac{1}{2} \left(1 + \mathrm{sign} \left(\sum_{n=0}^{N} T_n(0) u_n(t) \right) K_0 \right) \left(\sum_{n=0}^{N} T_n(0) u_n(t) \right)^2 \\
V_L &= P_L(t) - \frac{1}{2} \left(1 - \mathrm{sign} \left(\sum_{n=0}^{N} T_n(1) u_n(t) \right) K_L \right) \left(\sum_{n=0}^{N} T_n(1) u_n(t) \right)^2
\end{aligned} \tag{16}$$

The coupled system (13) is a system of first-order nonlinear differential-algebraic equations (DAE) of size $2M + 4(N+1)$. The state differential variables are $\mathbf{R}$, $\mathbf{Q}$, $\breve{\mathbf{U}}$, $\hat{\mathbf{U}}$, and the state algebraic variables are $\breve{\mathbf{P}}$, $\hat{\mathbf{P}}$. Moreover, we note that the DAE system is of differential index-2 [34], as the algebraic equations (flow continuity) do not contain the algebraic variables $\breve{\mathbf{P}}$, $\hat{\mathbf{P}}$ explicitly.

4. Method for the numerical continuation of periodic solutions

Contrary to previously derived formulations [16,22], the Galerkin approach presented here allows us to discretize the continuous 1-D problem into a set of nonlinear time-dependant equations with constant spatial operators. This makes it compatible for use in algorithms for the continuation of periodic solutions. As opposed to time-domain simulations, bifurcation analysis can provide a much broader view of the emerging limit-cycle oscillations (LCO), and how they vary as a function of specific control parameters.

In this work we have used the open-source software Manlab 4.0 [35] which combines the Harmonic Balance Method (HBM) for the time-discretization of the dynamical system with the Asymptotic Numerical Method (ANM) for the numerical continuation of the solution path. This software presents an efficient computational tool for the continuation of periodic solutions with respect to a control parameter, as well as their stability. Here we present only a brief explanation of the general continuation procedure used, but the interested reader can find more detailed descriptions in [28,36,37].

4.1. Harmonic balance method

The HBM is an efficient method for computing the periodic solutions of a smooth dynamical system [26], and it consist in expanding a T-periodic solution $\mathbf{g}(t)$ of a generic ODE/DAE system in the form of a Fourier series, truncated to H harmonics,

$$\mathbf{g}(t) = \sum_{h=-H}^{H} \mathbf{g}^{(h)} e^{\mathrm{i}h\omega t} = \mathbf{g}^{(0)} + \sum_{h=1}^{H} \left(\mathbf{g}_c^{(h)} \cos(h\omega t) + \mathbf{g}_s^{(h)} \sin(h\omega t)\right) \tag{17}$$

where the angular frequency of oscillation is $\omega = 2\pi/T$. After the appropriate Galerkin projection, the original ODE/DAE system of size N is then converted into an algebraic system of size $N(2H+1)$.

Additionally, for autonomous systems as is the case of the model studied here, the angular frequency ω of the periodic solution is not known *apriori*. That is, if $t \mapsto \mathbf{g}(t)$ is a periodic solution, then for all $\varphi \in \mathbb{R}$, $t \mapsto \mathbf{g}(t+\varphi)$ is also a periodic solution. To remove this phase invariance and account for the unknown ω, a so-called *phase equation* must be added to the algebraic system. For example, a commonly used condition is to assume a specific variable, say the first component $\mathbf{g}_1(t)$ of $\mathbf{g}(t)$, has a null derivative at $t = 0$, leading to

$$\sum_{h=-H}^{H} (ih\omega)\mathbf{g}_1^{(h)} = 0 \tag{18}$$

4.2. Asymptotic numerical method

The ANM is a continuation technique based on a high-order Taylor series expansions of the unknowns $\mathbf{g}(t)$ with respect to a control parameter λ [27]. The solution branches are computed in a step-by-step manner, as in classical predictor-corrector schemes [38], but because the accuracy of the high-order Taylor expansion is high, generally no correction is needed. Additionally, it provides a continuous description of the solution branch and also allows for the detection of bifurcations points automatically [39]. Consider the algebraic system

$$\mathbf{R}(\mathbf{g}, \lambda) = 0 \tag{19}$$

where $\mathbf{g} \in \mathbb{R}^N$ is a vector of unknowns and $\lambda \in \mathbb{R}$ is a control parameter, and $\mathbf{R} : \mathbb{R}^N$ is a real smooth function. Let $\mathbf{G}_0 = (\mathbf{g}_0, \lambda_0)$ be a regular solution of Eq. (19), and $\mathbf{G}_1 = (\mathbf{g}_1, \lambda_1)$ be a unitary tangent vector at point $\mathbf{G}_0$. Then, a pseudo-arc length parameter a can be introduced as

$$a = (\mathbf{g} - \mathbf{g}_0) \cdot \mathbf{g} + (\lambda - \lambda_0) \cdot \lambda = (\mathbf{G} - \mathbf{G}_0) \cdot \mathbf{G}_1 \tag{20}$$

Note that, the definition of a (20) serves as a closing equation for system (19). Then the search for a solution branch around $\mathbf{G}_0$ as an analytic function of a is given by the Taylor series expansion

$$\mathbf{G}(a) = \mathbf{G}_0 + a\mathbf{G}_1 + a^2\mathbf{G}_2 + a^3\mathbf{G}_3 + \ldots \tag{21}$$

The expansion (21) is replaced in Eq. (19) leading to

$$\mathbf{R}(\mathbf{G}(a)) = \mathbf{R}(\mathbf{G}_0) + a\mathbf{R}_1 + a^2\mathbf{R}_2 + a^3\mathbf{R}_3 + \ldots \tag{22}$$

where, truncated to an order p, we get

$$
\begin{aligned}
\mathbf{R}_1 &= \left.\frac{\partial \mathbf{R}}{\partial a}\right|_{a=0} = \frac{\partial \mathbf{R}}{\partial \mathbf{G}}\mathbf{G}_1 \\
\mathbf{R}_2 &= \left.\frac{1}{2}\frac{\partial^2 \mathbf{R}}{\partial a^2}\right|_{a=0} = \frac{\partial \mathbf{R}}{\partial \mathbf{G}}\mathbf{G}_2 - \mathbf{F}_2(\mathbf{G}_1) \\
\mathbf{R}_3 &= \left.\frac{1}{3!}\frac{\partial^3 \mathbf{R}}{\partial a^3}\right|_{a=0} = \frac{\partial \mathbf{R}}{\partial \mathbf{G}}\mathbf{G}_3 - \mathbf{F}_3(\mathbf{G}_1, \mathbf{G}_2) \\
&\vdots \\
\mathbf{R}_p &= \left.\frac{1}{p!}\frac{\partial^p \mathbf{R}}{\partial a^p}\right|_{a=0} = \frac{\partial \mathbf{R}}{\partial \mathbf{G}}\mathbf{G}_p - \mathbf{F}_p(\mathbf{G}_1, \ldots \mathbf{G}_{p-1})
\end{aligned}
\tag{23}
$$

with $\mathbf{F}_k$ being functions that depend only on previously computed terms in the series. Note that all equations in (23) share the same matrix to be inverted (i.e. the Jacobian at point $\mathbf{G}_0$). When the series (21) is computed up to a high-order p (here taken as 20), a working domain $[0, a_{\max}]$ can be defined as a function of a chosen residual tolerance ε. Assuming the approximation $\mathbf{R}(\mathbf{G}(a)) - \mathbf{R}(\mathbf{G}(0) = a^{p+1}\mathbf{R}_{p+1}$, this leads to

$$
a_{\max} = \left(\frac{\varepsilon}{\| \mathbf{R}_{p+1} \|}\right)^{\frac{1}{p+1}} \tag{24}
$$

Finally, an end point of each continuation step is computed $\mathbf{G}(a_{\max})$, which generally needs no correction, and serves as a starting point for the next continuation step.

Additionally, in the latest version of Manlab (4.0) a quadratic formalism is used that allows for the direct computation of the Jacobian matrix and the coefficients of the Taylor series [36]. This formalism is based on the definition of auxiliar variables (and equations) such that the augmented system contains only quadratic nonlinearities. Nevertheless, it can also deal with transcendental functions (sin, tan, exp, etc.), as described in [40]. This leads to an extremely efficient numerical tool for the continuation of periodic solutions, as well as their stability, using Hill's method [37].

5. On the question of hysteresis and sub-critical bifurcations

One of the most relevant open questions in the field of flow induced vibrations is related to the nature of the Hopf bifurcations (HB) they encounter. More specifically, numerous experiments [6,10,23,41] of fluttering cantilevered plates (or flags) under axial flow have shown the existence of bi-stable configurations, whereby under the same flow conditions a flexible membrane can be either oscillating (unstable equilibrium – periodic motion) or static (stable equilibrium). This leads to a hysteresis phenomenon whereby plates initially at rest will start oscillating at a specific critical velocity U_{c1}, while the same plate initially fluttering, will stop oscillating at a different critical velocity U_{c2}, where $U_{c2} < U_{c1}$. These observations suggest the existence of a sub-critical Hopf bifurcation and highlight the importance of initial conditions and/or the presence of external perturbations in the system. Understanding the physical nature of this

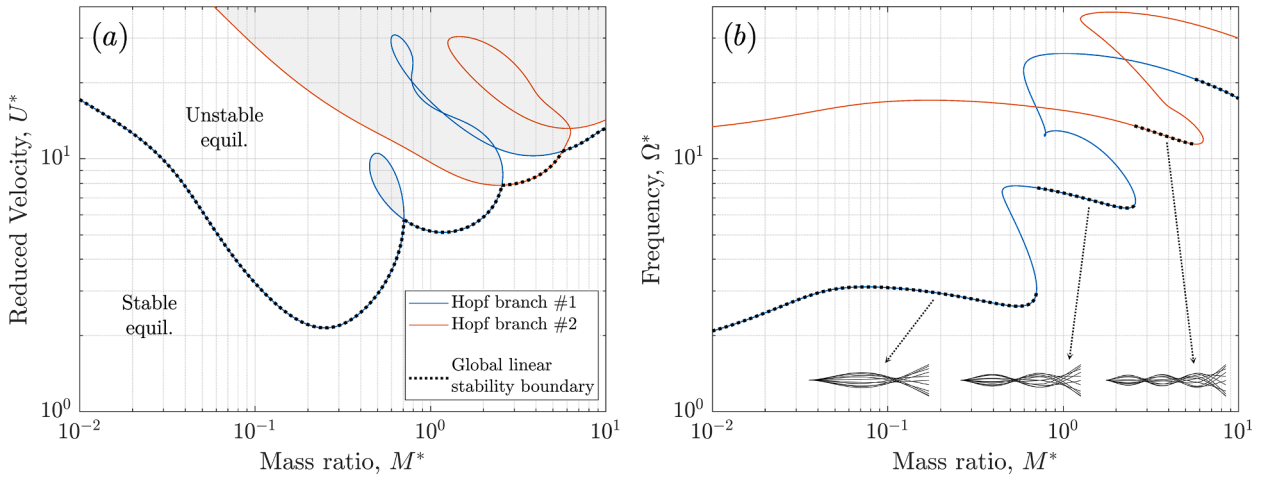

Fig. 2. Linear stability map for a system with constant symmetric channels and fixed parameters $H^* = 0.1$, $\zeta_n = 0.5\%$ and $f = 0$: (a) Hopf bifurcation branches and global linear stability boundary in the $M^* - U^*$ plane; (b) corresponding dimensionless critical frequencies $\Omega^* = \omega^*/\omega_0$ of the neutrally stable modes. The light grey areas in (a) indicate that multiple eigenvalues of the linearized system have positive real parts. The neutrally stable mode shapes are illustrated at the bottom of (b) for the first three steps of the "cascade".

phenomena has important practical implications as commonly used linear models will often predict non-oscillating stable regimes in configurations where oscillating ones co-exist, and can eventually arise.

The fact that the plethora of previously developed models are, for the most part, unable to predict bistable behaviour (see for example the interesting discussion in sections 3.2 and 3.4 of [10]), has led to an extensive discussion in literature for the last decades. By and large, the most common models found in literature use linearized equations of motion and are, by default, unable to capture eventual bistable behaviour. However, several attempts have been made to characterise the parametric regions in which bistable behaviour occurs using experiments [20,41] and, in fewer cases, temporal simulations using nonlinear models [10,23]. However, the general trend is that models often largely underestimate the width of the hysteresis loop $(U_{c1} - U_{c2})/U_{c1}$. This discrepancy has been attributed to flow nonlinear effects and viscosity, structural damping, unaccounted three-dimensional effects (either flow effects or 3-D plate deflections) as well as undesired flatness defects. Eloy et al. [42] have reported that plates with larger aspect ratios (width to length) lead to larger hysteresis loops and argued that, in ideal two-dimensional plates (i.e. beams, as assumed in most models), the Hopf bifurcation would be super-critical. More recently, the experimental results of Jankee and Barathram [41] suggested that the existence of hysteresis loops are impervious to the confinement ratio $H^* = (H_1 + H_2)/L$. Nevertheless, these systems generally depend on many dimensionless parameters and hence, the parametric-regions explored by experimental studies are often limited, and definite conclusions are not easily attained. In the following sections we present some modelling results and analysis that will hopefully clarify some of the aspects discussed above. Following reference studies, we consider the following dimensionless parameters: the fluid-beam mass-ratio M^*; confinement ratio H^*, structural damping ζ_n (assumed constant for all beam modes), frictional coefficient f (related to Reynolds number) and a reduced velocity

$$U^* = \frac{\left(\widehat{u}_0 + \breve{u}_0\right)}{2} \tag{25}$$

where $\widehat{u}_0$ and $\breve{u}_0$ represent the dimensionless entry velocities (normalized by $\omega_0 L$) on the lower and upper channels.

5.1. Constrained continuation and an "augmented" linear stability analysis

When studying the dynamics of flexible structures under axial flow, the linear stability analysis of the system is often the primary information to extract, as it allows us to distinguish between linearly stable equilibria where no motion occurs, and unstable ones where flutter oscillations or divergence arise. For this, the equations of motion are linearized (as done in [32] for the present model), and the eigenvalues of the linearized system are used to distinguish linearly stable/unstable equilibrium. Essentially, this allows us to identify Hopf bifurcations (when the eigenvalues of the coupled system have a null real part) and draw linear stability maps in multi-parameter spaces. A typical result is shown in Fig. 2(a), where the stability boundaries of the equilibrium solution in the $M^* - U^*$ plane are shown for a symmetric configuration with constant channel heights $H_1(x) = H_2(x) = H_1$ and fixed dimensionless parameters $H^* = 0.1$, $\zeta_n = 0.5\%$ and $f = 0$ (inviscid flow). Note that continuation methods, as the one described in Section 4.2, can also be used to calculate branches of Hopf bifurcations by adding constraint equations that define the HB (see for example the method described in [28]).

We notice there are two Hopf bifurcation branches whose combination forms a global linear stability boundary, i.e. the typical "cascading" frontier commonly found in literature. In this boundary, each step in the "cascade" corresponds to a change of shape of the primary unstable mode, as illustrated at the bottom of Fig. 2(b). Note as well that there are regions in the $M^* - U^*$ plane in which more than one eigenvalue of the system have positive real parts suggesting that, in these regions (in light grey), multiple periodic solutions can co-exist. The nature of the nonlinear behaviour occurring in these regions will be discussed in a later section.

We start by focusing on the post-critical behaviour found for relatively low mass-ratios. Fig. 3 shows the bifurcation diagrams at constant mass-ratios: (a) $M^* = 0.075$ and (b) $M^* = 0.2$. For $M^* = 0.2$, we see a super-critical bifurcation, where a stable branch of periodic solutions stems from the HB. On the other hand, for $M^* = 0.075$ the HB is sub-critical as the emerging branch of periodic

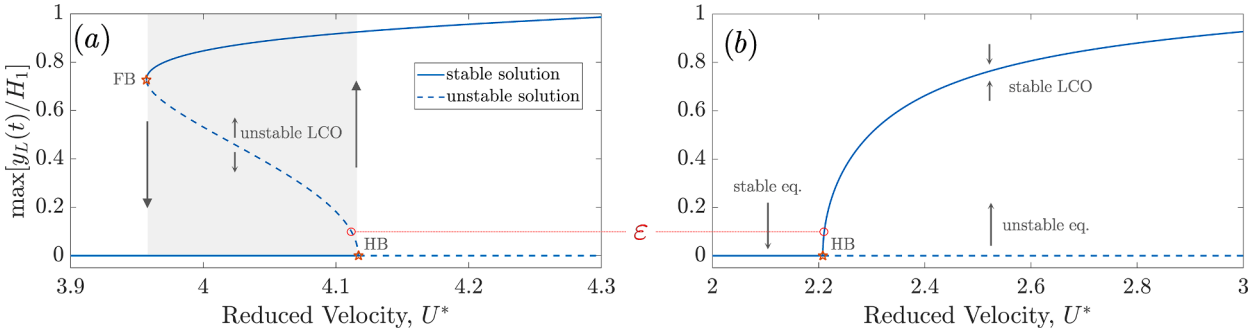

Fig. 3. Bifurcation diagrams of (a) a sub-critical HB at $M^* = 0.075$ and (b) a super-critical HB at $M^* = 0.2$. The light grey area in (a) corresponds to the bi-stable region where hysteresis loops will take place.

solutions is unstable. As usual in this type of sub-critical bifurcations, the solution branch is later stabilized through a fold bifurcation (FB) at a lower velocity. This type of sub-critical HB is likely the best explanation for the hysteresis effect commonly observed in experiments.

Even though linear stability analysis is, by default, unable to distinguish these two types of bifurcations, here we propose a method to calculate an "augmented" linear stability analysis. The general idea is similar to performing continuation of a HB branch, but instead of adding a constraint that defines the Hopf bifurcation, we add a constraint that fixes the amplitude of oscillation of a particular limit-cycle. Then, if we fix the amplitude of the oscillation to a small value ε (as qualitatively illustrated in Fig. 3), we will effectively follow a branch of periodic solutions that is arbitrarily close to the HB branch. More importantly however, we are then able to access their stability and hence distinguish between super-critical and sub-critical bifurcations.

In systems with cantilevered beams, maximal displacement during a limit-cycle oscillation will most often occur at the beam-tip ($x = 1$). Hence, we add to our system an equation defining the physical displacement of the beam-tip

$$y_L(t) = \sum_{m=1}^{M} \varphi_m(1) q_m(t) \tag{26}$$

Subsequently, we define our phase Eq. (18) such that the beam-tip velocity is zero at the beginning of the limit-cycle $\dot{y}_L(0) = 0$, i.e. beam-tip displacement is (locally) maximal (or minimal). Note that, at low amplitudes, oscillations will be nearly sinusoidal. Then, using the harmonic balance method, the beam-tip displacement is decomposed into

$$y_L(t) = \sum_{h=1}^{H} (a_h \cos(h\omega t) + b_h \sin(h\omega t)) \tag{27}$$

Finally, we can add a constraint equation that fixes the maximal amplitude of the beam-tip during a LCO to a small value ε by simply defining

$$y_L(0) = \sum_{h=1}^{H} a_h = \varepsilon \tag{28}$$

Naturally, this extra equation allows us to relax another parameter of the system and hence proceed with the continuation in a two-dimensional parameter space, like the $M^* - U^*$ plane as shown in the previous example. It is worth noting that Eq. (28) does not distinguish between a maximum and minimum. In a symmetric system, as is our case, both (symmetric) branches stemming from the Hopf bifurcation (maximum and minimum) will yield similar results. Nevertheless, for asymmetric configurations, using a solution with a maximum at $t = 0$ will suffice to initiate the continuation procedure.

5.2. *"Augmented" linear stability analysis of a two-mode system*

To examine the nature of the sub/super-critical HB and how they vary as a function of different dimensionless parameters of the system, here we present some results for a simplified configuration, considering a beam with only two *in-vacuo* modes, $M = 2$. This allows us to bypass more complex behaviour that arises when several modes are taken into account. Nevertheless, this assumption is deemed valid for relatively low mass-ratios M^*, where the main fluttering instability is dominated by the dynamics of the first two *in-vacuo* beam modes. In most applications in air, this will generally suffice.

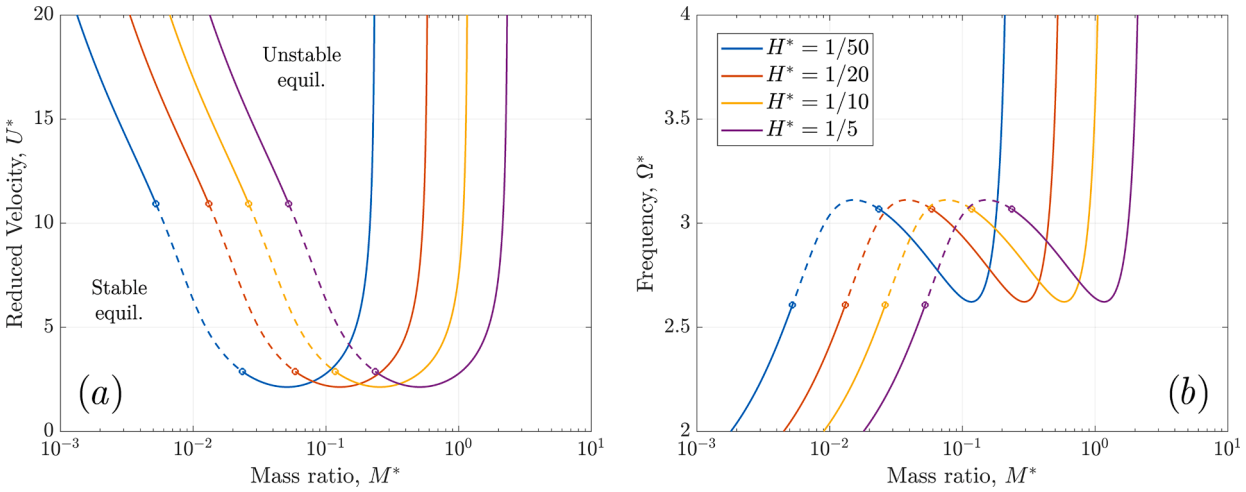

Fig. 4. Effect of confinement ratio H^* on (a) the linear stability boundaries in the $M^* - U^*$ plane and (b) corresponding frequencies of oscillation. Solid and dotted lines correspond to super-critical and sub-critical HB, respectively while the circles denote Bautin bifurcations.

In the following sub-sections, the method for the "augmented" linear stability described earlier was used to calculate the linear stability boundaries and their sub/super-critical character as a function of various dimensionless parameters. Throughout this section, the constraint amplitude was fixed at $\varepsilon/H_1 = 0.01$, the flow expansions truncated at $N = 8$ and the Fourier developments were truncated at $H = 5$.

5.2.1. The effect of confinement in inviscid flow

The effect of confinement on the stability boundaries of a cantilevered beam in confined flow was studied by Guo and Paidoussis [43] and Shoele and Mittal [17] using inviscid linearized flow equations, as well as in the work of Cisonni et al. [15] using a nonlinear 2-D viscous CFD model. All studies conclude that narrower confinements will have a destabilizing effect, at least for heavier beams (lower M^*). Additionally, results from the 2-D viscous model [15] underline how confinement will also affect viscosity related forces.

Here, we start by examining the simplest case, assuming inviscid flow ($f = 0$) in a symmetric configuration. The modal damping is assumed equal for both beam modes at $\zeta_1 = \zeta_2 = 0.5\%$ and the exit pressure-loss coefficient is set to $K_L = 1$. Fig. 4 shows the resulting linear stability boundaries in the $M^* - U^*$ plane for various confinement ratios H^*, as well as their corresponding critical dimensionless frequencies $\Omega^* = \Omega_0/\omega_0$, where Ω_0 is the frequency of the limit-cycle oscillation. The solid and dotted lines correspond to super-critical and sub-critical Hopf bifurcations, respectively, while the circles correspond to Bautin bifurcations (codimension-2 bifurcation points separating sub- from super-critical behaviour along the Hopf bifurcation branch).

Firstly, note that since we have considered a system with only two beam modes ($M = 2$), the stability boundaries in Fig. 4-(a) show only one "dip", corresponding to the first step in the "cascade" of Fig. 2. Overall, the results in Fig. 4, show that the stability boundaries do not change qualitatively, and simply shift towards lower mass-ratios M^* as the confinement H^* narrows. Effectively, according to our simplified model, a narrower confinement serves simply to increase the inertial effects of the fluid, i.e. decreasing the confinement ratio H^* will have the same effect as increasing the density of the fluid ρ. In fact, for the inviscid case ($f = 0$) results collapse if we consider the compound dimensionless parameter M^*/H^* (this parameter also appears in the analytical formulation derived in [22]). This conclusion is in general agreement with results from previous models [17,15]. However, the more complete 2-D viscous model found in [15] also predicts a slight overall lowering of the stability boundary when confinement is decreased, which is not captured by the current 1-D model. Nevertheless, this effect is secondary and the added flow inertia remains the dominant effect caused by confinement. Additionally, it must be noted that the bulk-flow equations used here assume small-to-moderate channel heights, and results for larger H^* do not converge to the unconfined (open flow) case. Comparisons to a 2-D viscous CFD model in [22], have suggested a range of validity for the current model at approximately $H^* < 1/5$. Presumably, when $H^* > 1/5$, two-dimensional flow effects became non-negligible and the stability boundaries from the 1-D model gradually diverge from those of the reference 2-D model.

Finally, we notice that sub-critical bifurcations occur only in a particular region of the stability boundary, at relatively low compound mass-ratios, i.e. $0.25 < M^*/H^* < 1.1$. These results are in agreement with the conclusions from a recent experimental study [41] which measured the effect of the mass and confinement ratios on the observed hysteretic behaviour, and suggest the *existence* of hysteresis is impervious to the effect of confinement. Furthermore, the region of M^* where the model predicts sub-critical bifurcations, agrees quantitatively with experimental observations (e.g. see Fig.7 on reference [41]).

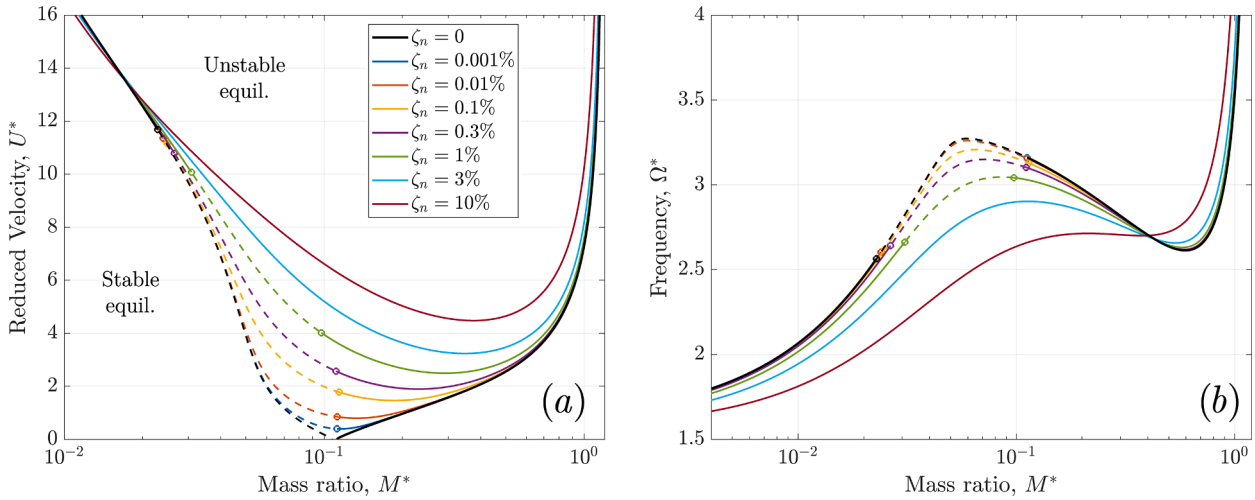

Fig. 5. Effect of structural damping ζ_n on (a) the linear stability boundaries in the $M^* - U^*$ plane and (b) corresponding frequencies of oscillation, in a symmetric system without frictional losses ($f = 0$), and confinement $H^* = 1/10$. Solid and dotted lines correspond to super-critical and sub-critical HB, respectively while the circles are Bautin bifurcations.

5.2.2. The effect of structural dissipation ζ_n

We now examine the effect of the structural damping ζ_n. Once again, we start by assuming inviscid flow ($f = 0$) and uniform structural damping $\zeta_1 = \zeta_2$. Here we fix the confinement ratio to $H^* = 1/10$ and the exit-loss coefficient to $K_L = 1$. Fig. 5 shows the linear stability boundaries in the $M^* - U^*$ plane for different values of ζ_n, as well as their corresponding frequencies.

Overall, results in Fig. 5 show that larger structural damping will stabilize the system, as stability boundaries are pushed towards larger flow velocities when modal damping ζ_n is increased. Furthermore, we notice that the region where sub-critical bifurcations occur do not change significantly for relatively low damping ($\zeta_n < 0.3\%$), remaining approximately between $0.25 < M^*/H^* < 1.1$. However, for larger damping ($\zeta_n = 1\%$) we notice the sub-critical region narrows and finally, for highly damped beams ($\zeta_n > 3\%$), it disappears completely, and bifurcations are super-critical for all M^*/H^*. This indicates that structural damping not only stabilises the system but also suppresses the occurrence of hysteresis.

Notably, we observe that, in the absence of structural damping ($\zeta_n = 0$), the model predicts a vanishingly small critical velocity (!) at a specific singular point $M^*/H^* \approx 1.1$. This result is clearly unrealistic and stems from the fact that no structural nor flow dissipation is taken into account. However surprising, similar results were obtained by Guo & Paidoussis in [43] when considering a conservative beam in inviscid flow. This indicates that, in the absence of dissipative terms inside the domain, a specific combination of mass and confinement ratios (M^*, H^*) will generate a naturally unstable (fluid-beam) coupled mode, where the irreversible energy transfer (from flow to structure) is unopposed. However, if either structural ζ_n or flow dissipation f are non-zero, finite critical velocities are obtained. Moreover, notice that this region of mass ratios also corresponds to the transitions between sub- and super-critical HB (Bautin bifurcations), both for conservative and nonconservative beams.

To provide a clearer perspective on the nature of the unstable fluttering beam, Fig. 6 illustrates the contribution of each *in-vacuo* beam mode in terms of its phase difference ϕ and its peak-amplitude ratio A_2/A_1, where $A_m = \max[q_m(t)]$. Additionally, the motion of the beam is illustrated for several example configurations M^* along the stability boundary.

As already stated by many previous studies, the flutter instability of a cantilevered beam occurs only if at least two *in-vacuo* beam modes are considered. Fig. 6(a) illustrates this point as the amplitude ratio never converges to either zero or infinity, underlining that the coupling between the two *in-vacuo* beam modes is essential to the flutter mechanism. We also note that, depending on the mass-ratio M^*, the (fluid-coupled) unstable mode is composed of different contributions from the two *in-vacuo* beam modes. For very small or very large mass ratios, the contribution of the 1st beam mode dominates, moving nearly in-phase ($\phi \sim 0$) for low mass ratios, and with $\phi \sim \pi/2$ for large mass ratios, with respect to the 2nd beam mode. At these extreme mass ratios, critical velocities are very large (see Fig. 5). On the other hand, the M^* region where reduced velocities U^* are lower (the "wells" in the $M^* - U^*$ boundaries) correspond to motions where the 2nd beam mode dominates. Note, in point 3 of Fig. 6(c), that the unstable coupled mode resembles almost exactly the 2nd *in-vacuo* beam mode. In these regions (minimum U^*), the two modes move nearly in phase for lightly damped beams. Additionally, for a conservative beam, the singular point with near-zero critical-velocity corresponds to an in-phase motion between the two *in-vacuo* beam modes.

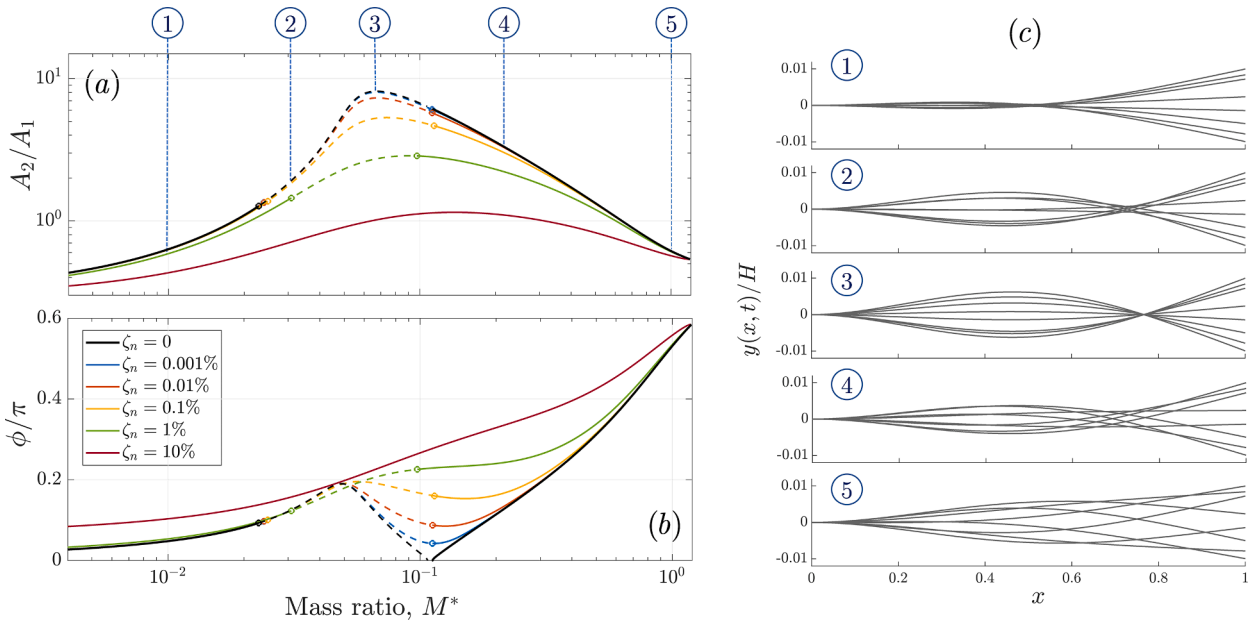

Fig. 6. Relative contribution of each in-vacuo beam mode in the unstable motion in terms of (a) the peak-amplitude ratio A_2/A_1 and (b) their phase difference; (c) illustrates the beam motion for various points (1–5) along the stability boundary for the conservative case $\zeta_n = 0$.

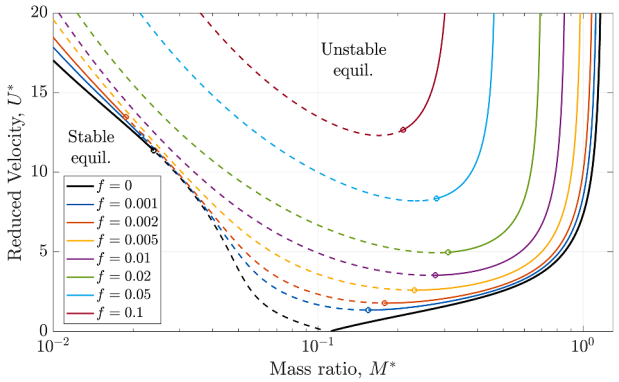

Fig. 7. Effect of the frictional coefficient f the linear stability boundaries of a symmetric system with a conservative beam ($\zeta_n = 0$) and confinement ratio $H^* = 1/10$. Solid and dotted lines correspond to super-critical and sub-critical HB, respectively while the circles are Bautin bifurcations.

5.2.3. *The effect of flow dissipation f*

Note that the distributed frictional term in the momentum Eq. (6) is given by $f(u_c^2/h_c)$, where f is a friction coefficient, related to the Reynolds number as illustrated in the classical Moody diagrams [31]. However, for vanishingly small amplitude beam motion (as is the case of the present quasi-linear analysis), this term can be approximated by considering only its static component, that is

$$u_c^2\left(\frac{f}{h_c}\right) = u_c^2\left(\frac{f}{\frac{H^*}{2} \pm \sum_{m=1}^{M} \varphi_m(x) q_m(t)}\right) \approx u_c^2\left(\frac{2f}{H^*}\right) \tag{29}$$

After the Galerkin projection, this approximation leads to extra nonlinear terms in the momentum equations in each channel, given by

$$\mathbf{G}_r = \left(\frac{2f}{H^*}\right) \sum_{n=0}^{N} \sum_{s=0}^{N} \left[\int_0^1 T_n(x) T_s(x) T_r(x) w(x) dx\right] u_n(t) u_s(t) \tag{30}$$

As this point it becomes clear that, when including frictional terms in the flow ($f > 0$), narrower passages (lower confinement ratios H^*) will increase the distributed pressure losses.

Fig. 7 shows the stability boundaries in the $M^* - U^*$ plane for various friction coefficients f, in a conservative beam ($\zeta_n = 0$). Similar to the effect of the structural dissipation, larger values of the friction coefficient f will stabilize the system. On the other hand, we notice they have a significant effect on the nature of the Hopf bifurcation. As f departs from zero, the Bautin bifurcations spread apart, enlarging the regions where sub-critical bifurcations occur. For $f \geq 0.005$, all HBs at lower mass-ratios are sub-critical, and become super-critical at relatively larger mass-ratios, $0.2 < M^* < 0.3$.

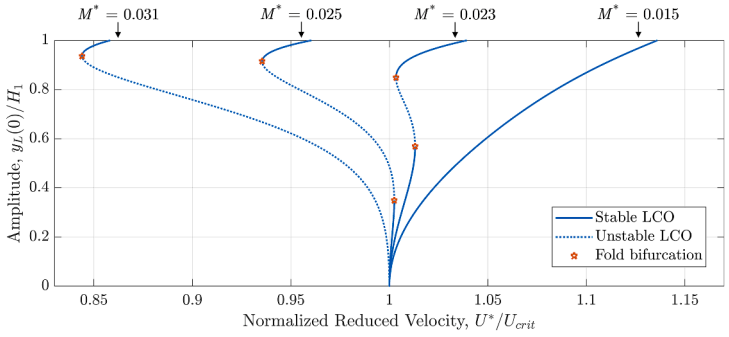

Fig. 8. Illustration of various cases of hysteresis: branches of periodic solutions in a symmetric system with $H^* = 0.1$, $\zeta_n = 0.5\%$, $f = 0$, $K_L = 1$, at various mass-ratios.

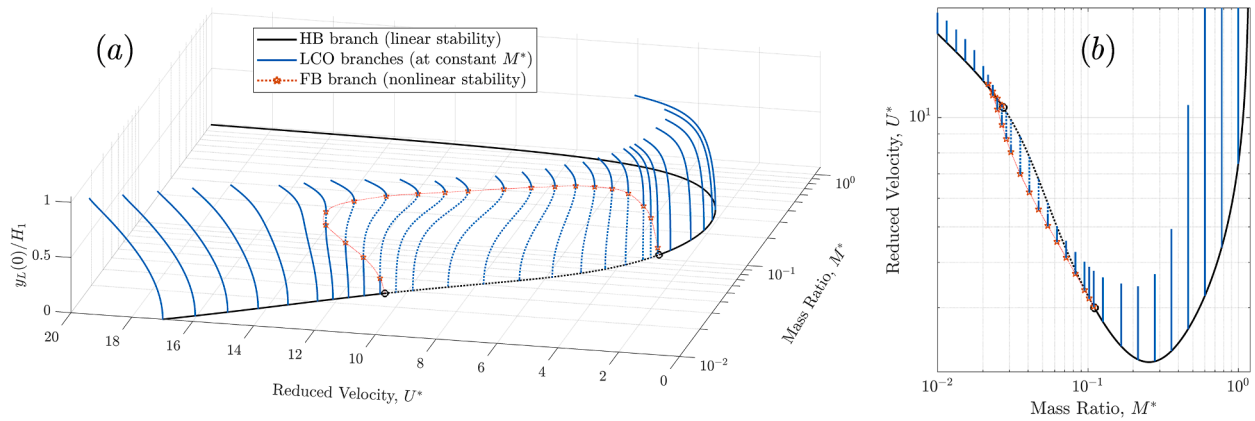

Fig. 9. (a) Three-dimensional view of the branches of periodic solutions (at constant M^*) stemming from the HB boundary, as well as (b) the corresponding top view ($M^* - U^*$ plane), for a symmetric system with $H^* = 0.1$, $\zeta_n = 0.5\%$, $f = 0$ and $K_L = 1$.

5.3. Nonlinear analysis of hysteresis

The "augmented" linear stability analysis presented above enables the distinction between sub- and super-critical Hopf bifurcations. However, it is worth noting that hysteretic behaviour is not unique to sub-critical HB, and it can also appear in super-critical ones. As an example, Fig. 8 shows several branches of periodic solutions for a symmetric system with $H^* = 0.1$, $\zeta_n = 0.5\%$, $f = 0$, and $K_L = 1$, in terms of the normalized reduced velocity U^*/U_{crit}, where U_{crit} is the critical velocity predicted by linear stability analysis. Here two-beam modes were considered $M = 2$, the flow field expansions were truncated at $N = 10$ and the harmonic series expansion was truncated at $H = 20$.

In Fig. 8 we notice that super-critical bifurcations can also lead to hysteretic behaviour, as a product of a double-fold bifurcation. Furthermore, the minimum velocity in the branch of periodic solutions can be larger or smaller than U_{crit}. It also illustrates that the transition from sub- to super-critical HB (Bautin bifurcation) does not necessarily mean the disappearance of hysteresis. To clarify the nature of this behaviour, several branches of periodic solutions were calculated for the same parameter configuration as above. Fig. 9 illustrates a three-dimensional bifurcation diagram where multiple solution branches (at constant M^*) are shown around the region where hysteresis is predicted.

From Fig. 9 is becomes clear that the Bautin bifurcations predicted in the (augmented) linear stability analysis are actually the birthing points of a fold-bifurcation branch. This FB branch travels the surface defined by the solution branches and outlines a frontier separating stable from unstable periodic solutions. Depending on the particular parameter configuration, this will generate the different types of bifurcations and hysteresis loops illustrated in Fig. 8.

It is clear that the analysis of this type of FB branch, and how it varies depending on different parameters of the system, is of paramount importance to understand and quantify the hysteresis phenomena. Even though in this work we do not conduct a detailed parametric analysis, the presented results serve as an example of potential avenues of research in the analysis of fluttering beams but also, more generally, in the field of flow-induced vibrations, where hysteresis occurs frequently in various contexts [44,45]. Note that here, the branch of FB was not calculated directly, but interpolated from the several fold bifurcations points. However, it is worth

Table 1
Range of hysteresis loops found by several experimental and numerical studies.

Type	Study	η (%)
Experimental	[3] Watanabe et al. (2002)	5 – 45
	[42] Eloy et al. (2008)	0 – 35
	[23] Eloy et al. (2012)	0 – 40
	[20] Gallegos & Sharma (2019)	15 – 48
	[41] Jankee et al. (2022)	20 – 70
Theoretical / Model	[24] Alben & Shelley (2008)	0 – 3.4
	[46] Michelin et al. (2008)	4.5
	[23] Eloy et al. (2012)	0 – 12.8
	Current model (2023)	0 – 22

mentioning that methods for the continuation of fold bifurcations have been developed, and can promptly be used for such type of analysis (see for example [28]).

5.4. Hysteresis loop width

As mentioned before, one of the open questions with regards to hysteresis has to do with the discrepancy between the hysteresis loop width, $\eta = (U_{c1} - U_{c2})/U_{c1}$, measured in experiments compared to modelling predictions. Concretely, models consistently underestimate the values observed in experiments, as illustrated in Table 1.

Solely from the example results shown above (Fig. 9), we already notice that the current model predicts hysteresis loop widths up to $\eta = 22\%$, which fall in the same order of magnitude as the values measured experimentally. In any case, further numerical investigations are necessary to explore the behaviour of the model in different parametric configurations.

As a final remark, the set of results presented here may help clarify some unanswered questions. Firstly, the present model is 1-D in nature, and hence its capacity to emulate sub-critical bifurcations and hysteresis is in contradiction with the hypothesis presented by Eloy et al. [42], where the authors suggest the nature of the bifurcation is super-critical, but two-dimensional plate deflections (unaccounted by the models) are the cause of hysteresis. Secondly, since geometric nonlinearities in the beam are not considered, results also suggest these might not be the root cause of hysteresis. Similarly, structural dissipation has also been mentioned as a potential cause for hysteresis [10]. However, our results show that sub-critical bifurcations occur in both conservative and non-conservative beams. Moreover, our results suggest that structural dissipation will actually supress sub-critical behaviour. In sum, the simplified configurations analysed here suggest that sub-critical bifurcations and hysteresis are result of flow nonlinearities. Furthermore, even though hysteretic behaviour is observed for inviscid flow, our numerical results indicate that the inclusion of nonlinear flow dissipation will promote the occurrence of sub-critical bifurcations, once again underlying the dominant role of flow nonlinearities in the phenomena of hysteresis.

6. Nonlinear dynamics of a system with many beam modes

6.1. Grazing boundary: separating LCOs with and without intermittent impacts

It is well known from experimental studies ([6,20,21]) that fluttering beams in confined flow will often lead to oscillations where the beam comes into contact with the channel walls. That is, these systems can produce periodic solutions both with and without intermittent impacts. It is worth noting that similar behaviour can be found in similar systems of flow induced vibrations- A pertinent example is that of a constrained pipe conveying internal flow [47,48]. Then, to provide an overview of the nonlinear behaviour of the system, it is useful to calculate a "grazing" boundary, i.e. the frontier separating periodic solutions with and without intermittent impacts. To this aim, the method presented in Section 5.1 for the "augmented" linear stability analysis, can also be adapted for the

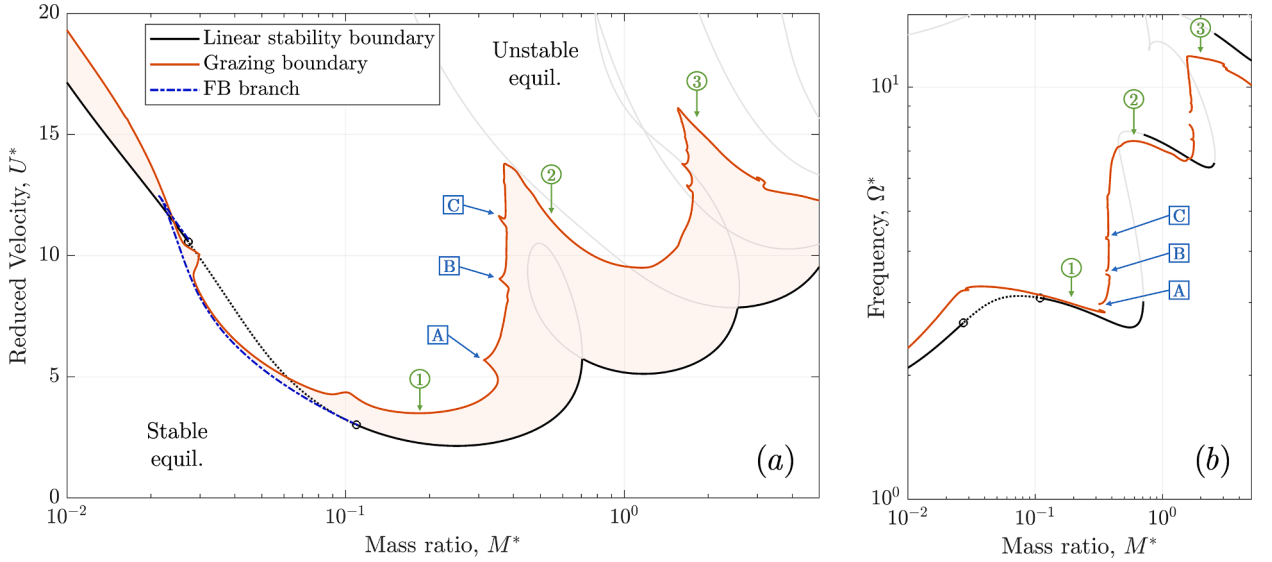

Fig. 10. (a) $M^* - U^*$ map illustrating the linear stability (black) and the near-grazing boundary (orange) for a symmetric system with $H^* = 0.1$, $\zeta_n = 0.5\%$, $f = 0$ and $K_L = 1$, as well as (b) its corresponding frequencies Ω^*. The blue dotted line shows the fold-bifurcation (FB) branch associated with the hysteresis region. The light orange filling describes the regions where limit cycles without impacts will occur. The light grey curves are the Hopf bifurcation branches, as shown in Fig. 2. Details of the solutions of the points indicated in green (1)-(3) and blue (A)-(C) are shown in Fig. 11 and Fig. 12, respectively.

estimation of the grazing boundary. While for the linear stability analysis we add a constraint Eq. (28) that fixes the amplitude of oscillation (beam-tip displacement) to a arbitrarily small value ε, here we will fix the maximum beam-tip displacement to the height of the channel $H_L = H_1(1)$. That is, we replace the constraint Eq. (28) by

$$y_L(0) = \sum_{h=-H}^{H} a_h = H_L - \varepsilon \tag{31}$$

where an arbitrarily small value ε is subtracted from H_L, effectively representing a *near*-grazing condition. In stating this condition (31), we assume that contact between the beam and the channel walls will occur firstly at the beam-tip $x = 1$. Although difficult to prove in a formal sense, experimental and modelling results all suggest that the largest displacement during an LCO will happen at the beam-tip and not along the beam. Hence, when considering channels of constant height, is seems reasonable to assume that impacts will occur initially at the tip. Then, similar to what was done in Section 5.1, we can proceed with the continuation of the near-grazing solution branches in a two-dimensional parameter space, like the usual $M^* - U^*$ plane.

For consistency, we present results for the same configuration as above, with fixed dimensionless parameters: $H^* = 0.1$, $\zeta_n = 0.5\%$, $f = 0$ and $K_L = 1$. For the spatial discretization, beam modes and the flow variable expansions were truncated at $M = 10$ and $N = 15$, respectively. For the temporal discretization, the number of harmonics were fixed at $H = 30$. This amounts to an algebraic system with approximately 5000 variables. Fig. 10 shows the calculated *near*-grazing boundary in the $M^* - U^*$ plane and corresponding frequencies, with $\varepsilon / H_L = 0.005$.

Overall, the results in Fig. 10(a) indicate that at low mass-ratios (heavy beams) the regions where LCOs without impacts occur are rather narrow, and contact with the channel walls will occur shortly after the equilibrium becomes unstable. On the other hand, at larger mass-ratios (light beams) there are larger regions with LCOs without impacts. This is likely explained by the fact that the inertia of a heavy fluttering beam will tend to outweigh the restoring forces from the (relatively) light fluid, while lighter beams will be more easily "pushed away" from the walls by the forces of a heavy fluid.

At low-mass ratios ($M^* < 0.3$), the behaviour is similar to what was found for the simplified system (considering only 2 beam modes) presented in Section 5.3, confirming that, for heavier beams, higher-order modes do not influence dynamics significantly (when impacts are not present).

The overall shape of the grazing boundary follows the same logic as the linear stability boundary, presenting a cascade-like structure, where different steps in the cascade represent changes in the primary unstable mode. To clarify, Fig. 11 shows details of the grazing solutions at different steps of the cascade (points (1)-(3) in Fig. 10). Similar to the results for the linear stability, the three steps of the cascade present beam motions with single-, double- or triple-neck solutions, where the first two, three and four *in-vacuo* beam modes dominate, respectively.

However, the grazing boundary also presents some more complex behaviour, including some discontinuities at the step-transitions (e.g. points (A)-(C) indicated in Fig. 10). To clarify, the solutions associated with points (A)-(C) are detailed in Fig. 12.

In can be seen that these small peaks effectively represent internal resonances in the system. Notice that, for point (A) the 3rd beam mode is very prominent (Fig. 12– bottom plot) and oscillates regularly, in a near sinusoidal fashion, at a frequency 3 times larger than the base frequency of the periodic motion Ω_0. Similarly, at points (B) and (C), the 4th and 5th beam modes oscillate at frequencies approximately 5 and 7 times the base frequency, respectively. This suggests that at these junctures, the frequency of higher-order

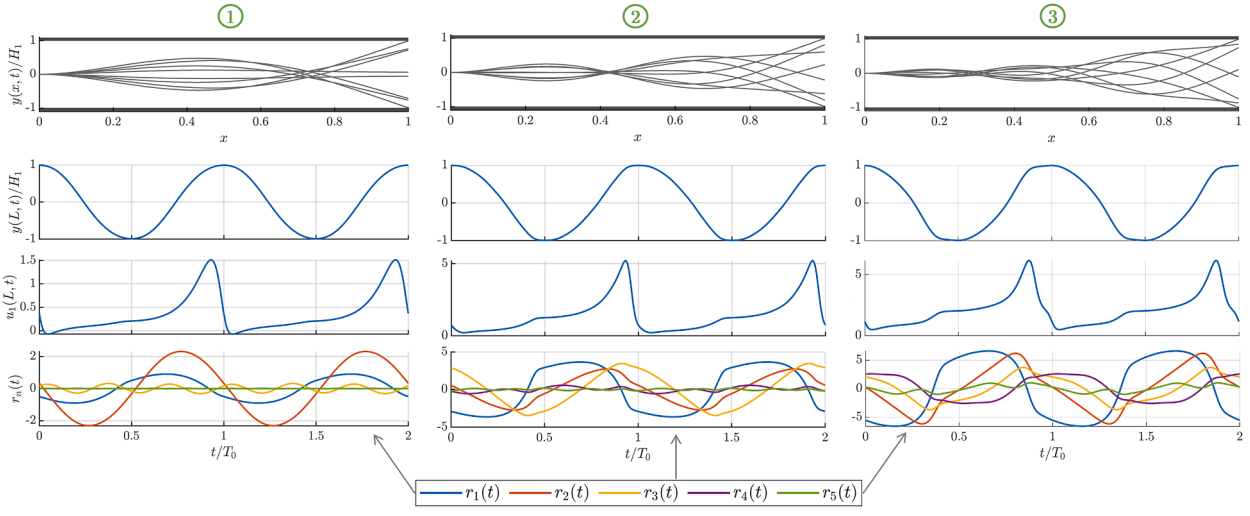

Fig. 11. Grazing solutions associated with different steps in the cascade (points (1)-(3) indicated in Fig. 10). Snapshots of the beam motion (top); temporal evolution of the beam-tip displacement $y_L(t)/H_1$(top-centre), the exit flow velocity $u_1(1,t)$ at the upper channel (bottom-centre) and the modal velocities of the first 5 beam modes (bottom). Note that the time is normalized by the period of the limit-cycle T_0, and the frequencies of the three solutions differ significantly, as seen in Fig. 10.

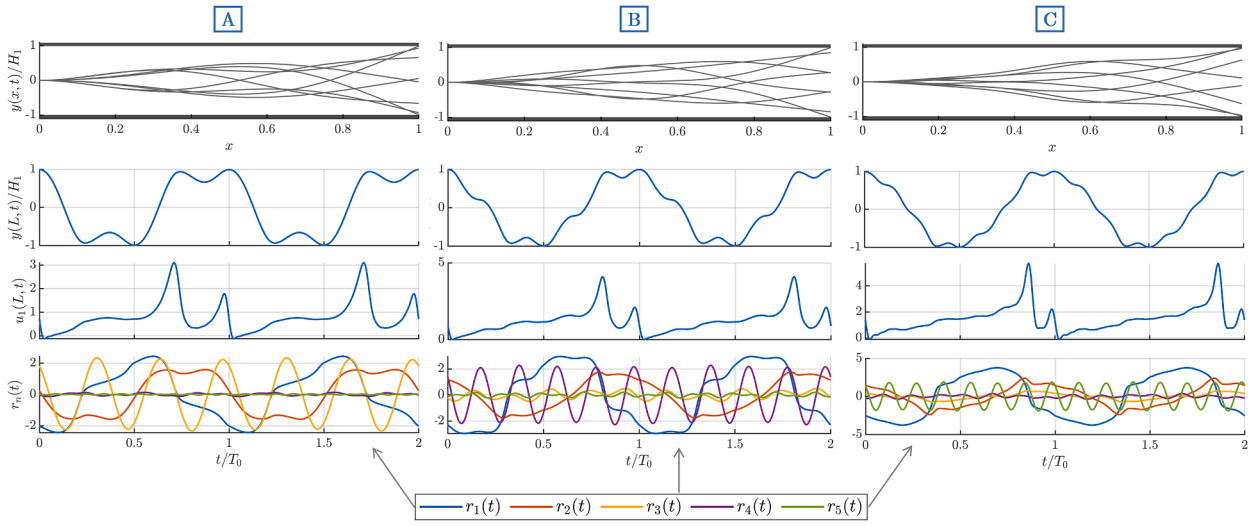

Fig. 12. Grazing solutions associated with different internal resonances (points (A)-(C) indicated in Fig. 10). Snapshots of the beam motion (top); temporal evolution of the beam-tip displacement $y_L(t)/H_1$ (upper-central), the exit flow velocity $u_1(1,t)$ at the upper channel (lower-central) and the modal velocities of the first 5 beam modes (bottom).

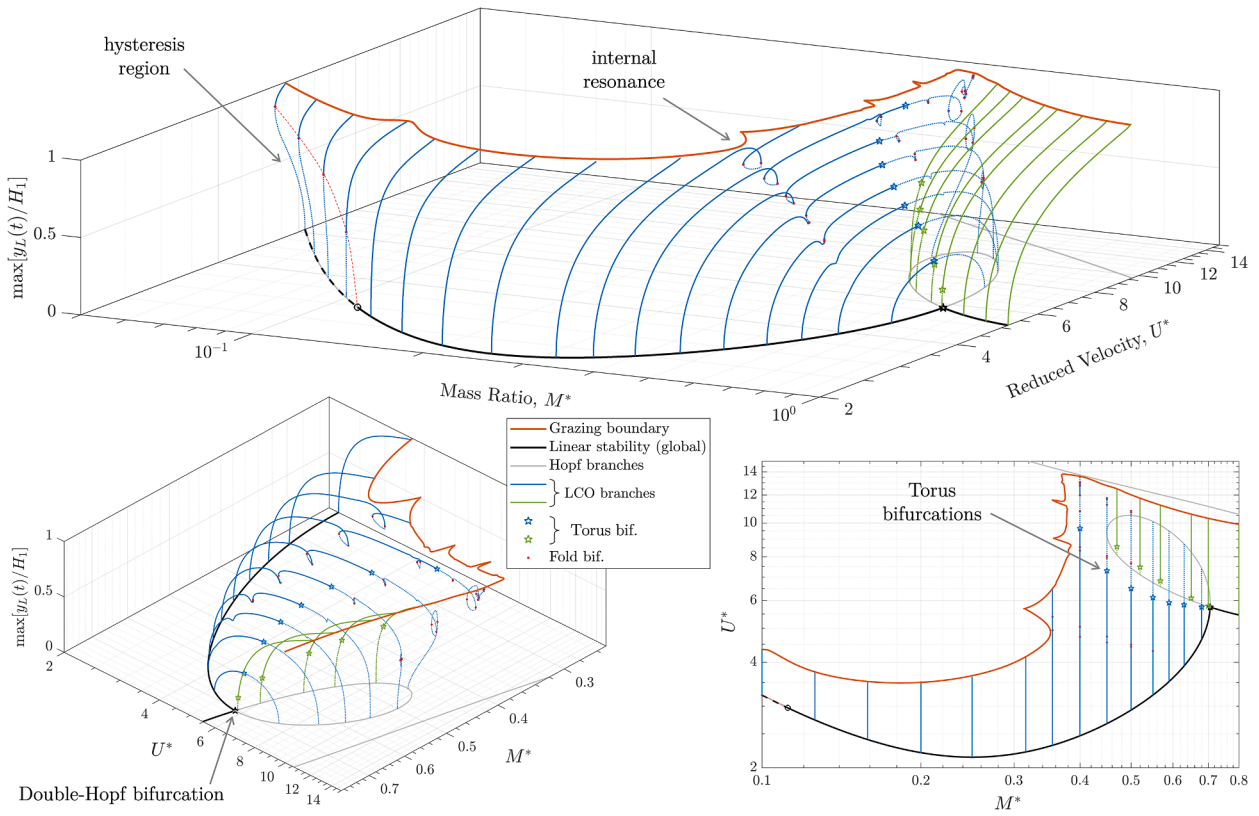

Fig. 13. Various perspectives of a three-dimensional bifurcation diagram showing branches of periodic solutions at constant M^* (blue and green lines) stemming from the calculated Hopf bifurcations, at low-moderate mass-ratios ($0.05 < M^* < 1$). The black and orange lines denote the (global) linear stability and grazing boundaries, respectively.

(fluid-loaded) beam modes $\widetilde{\omega}_{3,4,5}$ are close to a multiple integer of the base frequency. That is, at point (A) $\widetilde{\omega}_3 \approx 3\Omega_0$, at point (B) $\widetilde{\omega}_4 \approx 5\Omega_0$ and at point (C) $\widetilde{\omega}_5 \approx 7\Omega_0$, leading to larger responses of higher-order modes and naturally, more complex beam motions. It is unsurprising that these internal resonances occur at the step-transitions of the cascade, since these regions are associated with an abrupt change in the frequency of the periodic solution (see Fig. 10(b)). Notably, at the grazing boundary, these internal resonances present solutions where the beam-tip grazes the channel walls twice during each period, as shown in Fig. 12. Furthermore, because the system is symmetric, the spectrum of the beam motion contains only odd harmonics, and hence internal resonances occur only at odd multiples of the base frequency. Nevertheless, it is likely that an asymmetric system, where even harmonics are also present, will generate additional internal resonances.

It is also worthwhile analysing the fluid dynamics associated with the grazing solutions, represented in Fig. 11 and Fig. 12 by the exit velocity $u_1(1,t)$ in the upper channel (note that, due to symmetry, the velocities in the lower channel will be similar, with a half-period lag). As the beam-tip approaches the upper wall, the exit flow velocity increases and subsequently decreases abruptly right before the beam-tip reaches its maximum displacement. This sudden decrease in flow velocity is a product of a squeeze-like effect caused by the beam inertia on the (incompressible) fluid as well as the nonlinear flow dissipation governed by head-loss term $u|u|K_L$, and leads to local velocities close to zero, and even reversed flow in some cases. Once the constriction starts to widen, flow velocities are gradually restored. In the solutions presented in Fig. 12 this process is repeated twice during each cycle.

6.2. Dynamics near the modal-transition region

Once the frontier separating periodic solutions with and without intermittent impacts is defined, we can now analyse in more detail the nature of the LCOs in the contactless regions. Namely, we now examine the solutions at moderate mass-ratios $(0.1 < M^* < 1)$, where the first cascade transition occurs and notably, where linear stability analysis predicts regions with multiple unstable equilibria. The 3-D plots shown in Fig. 13 give an overview of the periodic solutions occurring in this region. Dimensionless and discretization parameters were taken as in the previous sub-section.

The overview presented in Fig. 13 shows that away from the step-transition, periodic solutions tend to have a fairly regular pattern, simply increasing in amplitude with increasing velocity U^*, with no relevant qualitative changes. However, near the step-transitions more complex dynamical behaviour arises. These include, for example (1) loops in the solution branches caused by internal resonances, (2) regions where multiple solutions co-exist and (3) torus bifurcations and associated quasi-periodic solutions. In the following we examine these phenomena in more detail.

In Fig. 13 we note several sequences of loops in the solution branches (blue), with fold bifurcations located at the turning points. As was discussed previously, these loops are associated with internal resonances of the system. As solutions come closer to the grazing boundary (where beam motion is of larger amplitude), the internal resonance loops become more pronounced. To better illustrate the phenomena, Fig. 14 shows the distribution of mean modal energy E_m in the beam along the solution branch at constant mass-ratio $M^* = 0.4$. Note that E_m is dimensionless, normalized by the reference energy $E_0 = m_0\omega_0^2 L^2$, and given explicitly by

$$E_m = \left(\frac{m_m}{2}\right)\left(\frac{1}{T_0}\right)\int_0^{T_0}\left(\dot{q}_m^2(t) + \omega_m^2 q_m^2(t)\right)dt \tag{32}$$

where $q_m(t)$ and $\dot{q}_m(t)$ can be calculated directly using the coefficients from the harmonic balance expansion (as in Eq. (17)).

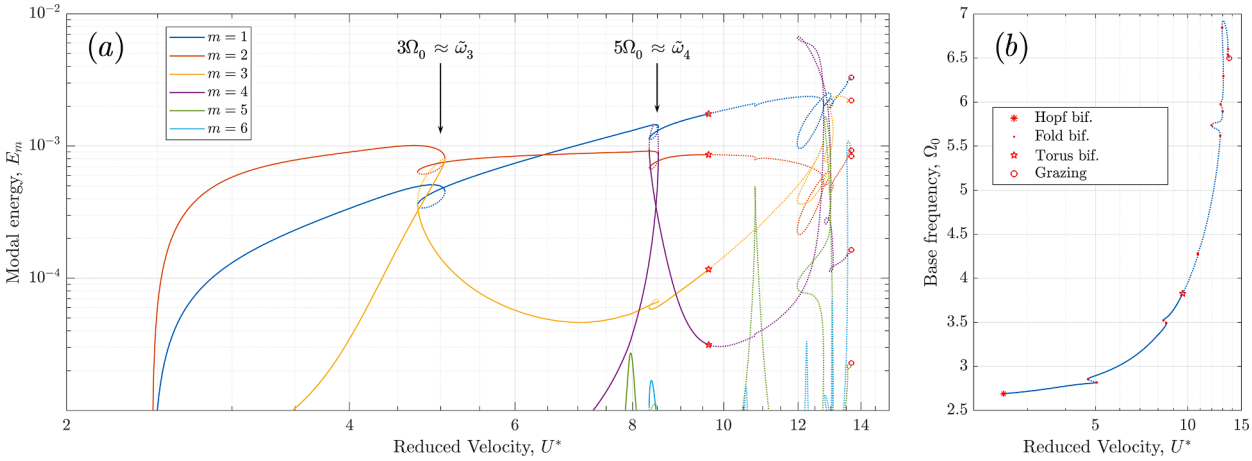

Fig. 14. Illustration of internal resonances. (a) Evolution of the modal energy distribution in the beam as a function of the reduced velocity U^* along the solution branch at $M^* = 0.4$; and (b) the corresponding frequency. Solid and dotted lines denote stable and unstable solutions, respectively.

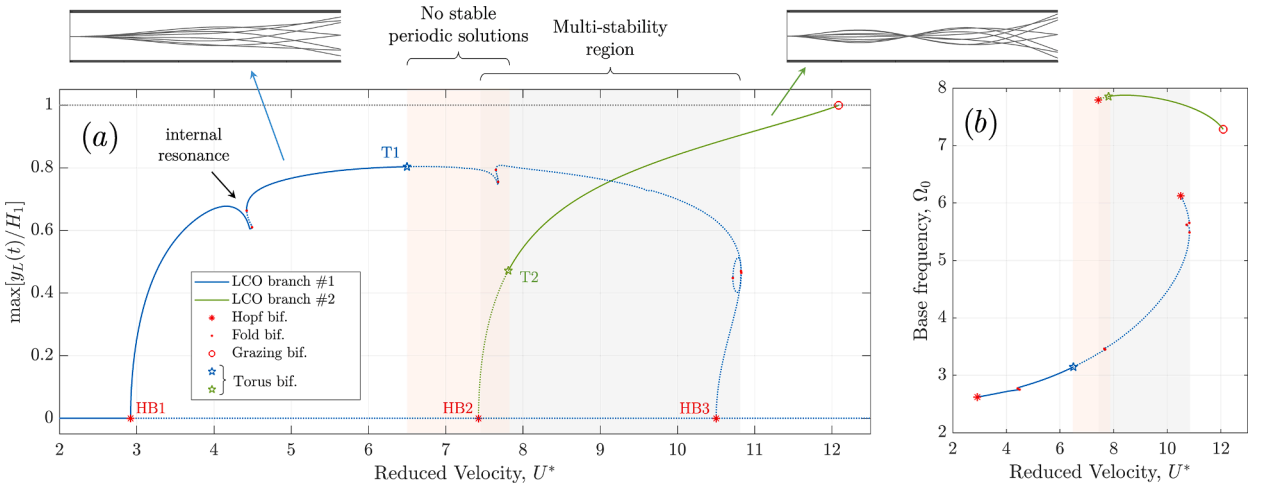

Fig. 15. Illustration of the mode-transition and multi-stability regions: (a) bifurcation diagram at constant mass-ratio $M^* = 0.5$, illustrating the two branches of periodic solutions with respect to the reduced velocity U^*; (b) evolution of the base frequency associated with each solution branch. The light-orange area indicates that no stable periodic solution exists, while the light-grey area denotes that more than one solution branch exists, either stable or unstable.

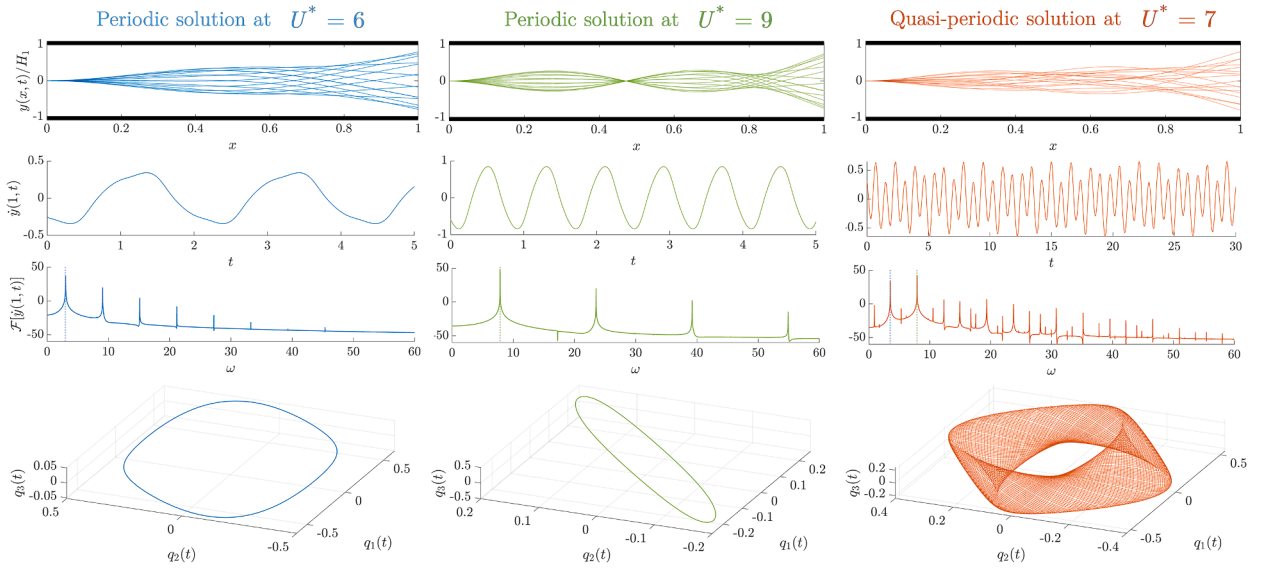

Fig. 16. Resulting nonlinear motions for a system with $M^* = 0.5$ and three different velocities $U^* = [6,\ 9,\ 7]$. From top to bottom: snapshots of the beam motion; temporal evolution of the beam-tip velocity $\dot{y}(1,t)$; spectra of the beam-tip velocity; phase-portrait in the modal displacement plane $[q_1(t),\ q_2(t),\ q_3(t)]$.

We note that the underlying periodic solution is dominated by the first two beam modes (blue and red lines in Fig. 14). As U^* increases, the frequency Ω_0 also increases and, at given moments, higher-order modes are locally excited. The internal resonances $\widetilde{\omega}_3/\Omega_0 = 3$ and $\widetilde{\omega}_4/\Omega_0 = 5$ are highlighted in Fig. 14, however, many other internal resonances occur at larger velocities. Nevertheless, the solution branch loses its stability through a torus bifurcation at around $U^* = 9.7$. Hence, solutions at $U^* > 9.7$ will likely lead to quasi-periodic motions (this will be discussed in detail subsequently).

Notably, Fig. 13 illustrates the nature of the change in periodic solutions as mass-ratios pass through the cascade's step-transition. The periodic solutions where the first two beam modes are dominant (blue lines) start to decrease in amplitude as mass-ratios increases, and eventually disappear at the turning point of the Hopf branch ($M^* \approx 0.7$). Meanwhile, a new surface of periodic solutions

emerges at $M^* \approx 0.45$ (green lines), corresponding to periodic solutions where the third beam mode is dominant. Beyond the step-transition ($M^* > 0.7$), this second surface of solutions (green) is unique. However, there are overlapping regions where both solution branches co-exist. To clarify, Fig. 15 shows the evolution of the two solution branches as a function of the reduced velocity U^*, for a constant mass-ratio $M^* = 0.5$.

Then, once the equilibrium becomes unstable, we can then identify three qualitatively different scenarios:

1. *Single stable periodic solution*: where typical (periodic) limit-cycle oscillations will arise;
2. *No stable periodic solutions*: will generally lead to quasi-periodic oscillations, i.e. motion whose spectra is composed by a linear combinations two (or more) harmonic series whose base frequencies are incommensurable;
3. *Multiple periodic solutions, stable or unstable, co-exist:* the system dynamics will be governed by initial conditions and can converge to either periodic or quasi-periodic motion.

To clarify the nature of the ensuing periodic and quasi-periodic regimes, Fig. 16 shows details of three solutions obtain via temporal integration with $U^* = [6,\ 9,\ 7]$. Initial conditions were set at the equilibrium position (beam at rest and steady flow) and a small perturbation force was applied to induce flutter. Fig. 16 shows the resulting periodic/quasi-periodic solutions sometime after motion stabilises.

At $U^* = 6$, since the only stable solution is periodic, the temporal simulation naturally converged to a limit cycle oscillation associated with the single-neck beam motion (blue branch in Fig. 15). As predicted by the continuation results, its frequency of oscillation was at $\Omega_0 = 3.03$. At $U^* = 9$, the system is in a multi-stable region and the chosen initial conditions led the motion towards the stable periodic solution of the double-neck type (green branch in Fig. 15), with a base frequency of $\Omega_0 = 7.84$. However, we constate that the dynamics are rather sensitive to initial conditions, and for example, simulations with larger amplitude perturbations led to quasi-periodic regimes. Due to the symmetry of the system, the frequency content of both these periodic solutions contains only odd harmonics of their respective frequencies, i.e. $(2n-1)\Omega_0$. Finally, at $U^* = 7$, the system has no stable periodic solutions and temporal simulation eventually converged to a stable quasi-periodic motion. As usual, the (3D) orbit of the quasi-periodic solution does not remain in a line, as in the periodic cases, but rather in a torus (closed invariant curve). The spatial distribution of the beam motion in the quasi-periodic regime is less regular but can be roughly regarded as a combination of the single- and double-neck periodic solutions. In fact, its frequency content contains a linear combination of two base frequencies, $\Omega_1 = 3.51$ and $\Omega_1 = 7.92$, which are close to those found for the associated periodic regimes. For the quasi-periodic solutions, the spectrum of the beam-tip velocity shows peaks at

$$\omega_{n,m} = |\pm n\,\Omega_1 \pm m\,\Omega_2| \quad \text{for} \quad n, m = 1, 2, 3... \tag{33}$$

However, additionally, the harmonics $\omega_{n,m}$ where $(-1)^n = (-1)^m$ are null. In analogy to the lack of even harmonics in periodic solutions of symmetric systems, this condition is also a property of quasi-periodic oscillations in symmetric systems.

It is also worthwhile discussing the origin of the torus bifurcations. From Fig. 13 it becomes evident that these stem from a double-Hopf bifurcation, i.e. the crossing point on the Hopf branch, where the critical equilibrium has two pairs of purely imaginary eigenvalues (black star in Fig. 13). Generally, two torus branches emanate from a double-Hopf point [25]. This is illustrated clearly in

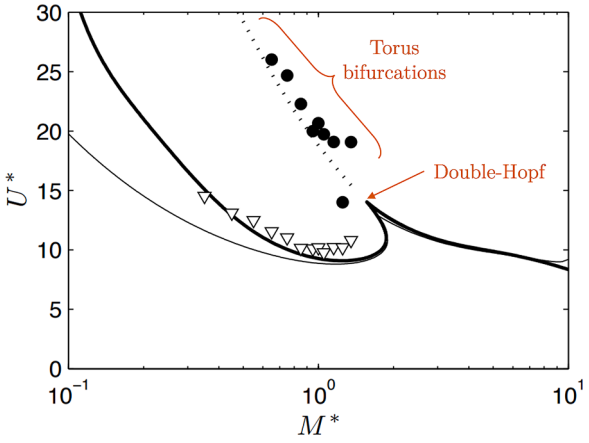

Fig. 17. Experimental results from Eloy et al. [23] for a plate in unconfined axial flow. The measured critical velocities for the start of oscillations are shown by the triangles, while the circles mark the loss of periodicity. The solid lines represent the Hopf bifurcations using a conservative (thin) and dissipative models (thick). The annotations in orange were appended by the present authors to the original figure in [23].

Fig. 13, where two branches evidently travel in each surface of solutions (both blue and green). Each torus bifurcation in the solution branch will generate an invariant torus on which quasi-periodic orbits will develop. This analysis brings a new perspective on the nonlinear dynamics of flexible beams in axial flow, both in confined and open flow configurations. Effectively, the discontinuities in the common cascading linear-stability boundaries represent double-Hopf bifurcations and hence, it is expected that quasi-periodic oscillations will occur frequently near these regions of the parameter space. For example, the experimental results from Eloy et al. [23], where the dynamics of a plate in unconfined axial flow is studied, show exactly this behaviour. Fig. 17 shows their measured critical velocities for the threshold of periodic oscillations (triangles) as well as the velocities where the fluttering motion loses periodicity (circles). Notably, the trend of the measured critical velocities for loss of periodicity compares remarkably well with the torus bifurcations shown in our numerical results (Fig. 13).

7. Conclusion

In this work, the nonlinear dynamics of a flexible beam in axial flow were studied numerically through bifurcation analysis. A one-dimensional model was considered, where a modal beam is surrounded by confined flow on both sides. The flow was modelled using bulk-flow equations which include localised and distributed head-loss terms that encapsulate, in a compact manner, nonlinear dissipative flow effects occurring inside and outside the domain. Contrary to previous studies on the subject, which relied on the temporal integration of the equations of motion, here we have resorted to methods for the continuation of periodic solutions combined with the harmonic balance method. Aside from being computational efficient, these allow for a thorough analysis of the bifurcations occurring in these systems and a more comprehensive overview of its dynamics by following solution paths in terms of one or more system parameters.

The question of hysteresis and sub-critical bifurcations was discussed extensively. Namely, a method for an "augmented" linear stability analysis was proposed, where not only Hopf bifurcation branches can be calculated with respect to two system parameters, but their super-/sub-critical nature can also be easily distinguished, as well as the calculation of Bautin bifurcations. Our numerical results indicate that structural damping not only stabilises the system (larger critical velocities), but also tends to supress sub-critical behaviour. Additionally, even though sub-critical behaviour was found for inviscid flow, the inclusion of nonlinear flow dissipation (distributed frictional term) will favour sub-critical behaviour and hysteresis loops. Our results clearly suggest that sub-criticality and hysteresis are a product of flow nonlinearities, as no other nonlinearity is accounted in this one-dimensional model. This comes in contrast with previous hypotheses [10,42] which attempted to explain the phenomena through structural nonlinearities, flow or structural three-dimensional effects, undesired planeity defects, etc.

Grazing boundaries were also calculated, allowing the separation of parameter-regions where limit-cycle oscillations with and without impacts will occur. Our results indicate that heavier beams will tend to have narrow regions with contactless LCOs, i.e. limit-cycles with intermittent impacts between the beam and the channels walls will arise promptly after the equilibrium becomes unstable. As a note, future work by the authors will deal with the inclusion of a contact model, and the bifurcation analysis of solutions with intermittent impacts.

A detailed mapping of the system dynamics in the $M^* - U^*$ plane revealed a number of complex nonlinear phenomena like internal resonances, multi-stable configurations and quasi-periodic dynamics. Notably, a feature common to both open- and channel-flow configurations, is the occurrence of double-Hopf bifurcations. These represent the "modal-transitions" commonly mentioned in previous studies, where the primary unstable fluttering mode changes shape. However, our results show that such bifurcation points also give birth to torus branches, which lead to a loss of stability of the periodic solutions and generate quasi-periodic (and potentially chaotic) dynamics.

This work presented an analysis of the bifurcations and illustrated the rich dynamical behaviour occurring in systems of flexible beams in axial flow. Aside from providing novel insights into the physics of fluttering beams and suggesting news avenues of research, is it hoped that the methods and results presented here can stimulate similar studies in the field of flow-induced vibrations.

CRediT authorship contribution statement

Filipe Soares: Methodology, Software, Data curation, Formal analysis, Visualization, Writing – original draft, Writing – review & editing. **Christophe Vergez:** Conceptualization, Methodology, Supervision, Writing – review & editing. **Jose Antunes:** Formal analysis, Supervision, Writing – review & editing. **Bruno Cochelin:** Conceptualization, Writing – review & editing. **Vincent Debut:** Supervision, Writing – review & editing. **Fabrice Silva:** Writing – review & editing.

Declaration of Competing Interest

The authors declare that they have no known competing financial interests or personal relationships that could have appeared to influence the work reported in this paper.

Data availability

Data will be made available on request.

Acknowledgements

The authors gratefully acknowledge the financial support given by "Fundação para a Ciência e Tecnologia" (FCT – Portugal) through the PhD grant referenced SFRH/BD/140598/2018.

References

[1] M.P. Paidoussis, Fluid-Structure Interactions: Slender Structures and Axial Flow, Academic Press, San Diego, California, 2004.
[2] Z. Li, S. Zhou, Z. Yang, Recent progress on flutter-based wind energy harvesting, Int. J. mechan. syst. dynamics 2 (2022) 82–98.
[3] Y. Watanabe, S. Suzuki, M. Sugihara, Y. Sueoka, An experimental study of paper flutter, J. Fluids Struct. 16 (4) (2002) 529–542.
[4] Y. Chai, W. Gao, B. Ankay, F. Li, C. Zhang, Aeroelastic analysis and flutter control of wings and panels: a review, Int. J. mechan. syst. dynamics 1 (2021) 5–34.
[5] F. Avanzini, M. Walstijn, Modelling the mechanical response of the reed-mouthpiece-lip system of a clarinet. Part 1: a one-dimensional distributed model, Acta Acust. United Acust. 90 (2004) 537–547.
[6] Y. Aurégan, C. Depollier, Snoring: linear stability analysis and in-vitro experiments, J. Sound Vib. 188 (1) (1995) 39–54.
[7] E. Virot, X. Amandolese, P. Hémon, Fluttering flags: an experimental study of fluid forces, J. Fluids Struct. 43 (2013) 385–401.
[8] H. Abderrahmane, M. Paidoussis, Flapping dynamics of a flexible filament, Phys. Rev. E 84 (066604) (2011).
[9] M. Chen, L.-B. Jia, Y.-F. Wu, X.-Z. Yin, Y.-B. Ma, Bifurcation an chaos of a flag in an insviscid flow, J. Fluids Struct. 45 (2014) 124–137.
[10] L. Tang, M. Paidoussis, On the instability and post-critical behaviour of two-dimensional cantilevered flexible plates in axial flow, J. Sound Vib. 305 (2007) 97–115.
[11] Y. Yu, Y. Liu, X. Amandolese, A review on fluid-induced flag vibrations, Appl. Mech. Rev. 71 (010801) (2019).
[12] H. Nagakura, S. Kaneko, Stability of a cantiliver beam subject to one-dimensional leakage flow, in: Proceedings Asia-Pacific Conference `93, Kitakyushiu, Japan 1, 1993, pp. 352–359.
[13] D. Tang, H. Yamamoto, E. Dowell, Flutter and limit cycle oscillations of two-dimensional panels in three-dimensional axial flow, J. Fluids Struct. 17 (2003) 225–242.
[14] W.-X. Huang, H.J. Sung, Three-dimensional simulation of a flapping flag in uniform flow, J. Fluid Mech. 653 (2010) 301–336.
[15] J. Cisonni, A. Lucey, N. Elliot, M. Heil, The stability of a flexible cantilever in viscous channel flow, J. Sound Vib. (2017).
[16] L.P. Tosi, T. Colonious, Modelling and simulation of a fluttering cantilever in channel flow, J. Fluids Struct. 89 (2019) 174–190.
[17] K. Shoele, R. Mittal, Flutter instability of a thin flexible plate in a channel, J. Fluid Mech. 786 (2016) 29–46.
[18] T. Balint, A. Lucey, Instability of a cantilevered flexible plate in viscous channel flow, J. Fluids Struct. 20 (2005) 893–912.
[19] X. Wu, S. Kaneko, Linear and Nonlinear analyses of sheet flutter induced by leakage flow, J. Fluids Struct. 20 (2005) 927–948.
[20] R. Gallegos, R. Sharmaa, Small flags in rectangular channels: dynamics and mean wake characteristics, Int. J. Mech. Sci. 155 (2019) 518–535.
[21] J. Lee, D. Kim, H.-Y. Kim, Contact behavior of a fluttering flag with an adjacent plate, Phys. Fluids 33 (2021).
[22] F. Soares, J. Antunes, V. Debut, C. Vergez, B. Cochelin, F. Silva, A nonlinear analytical formulation for the 1D modelling of a flexible beam in channel flow, J. Fluids Struct. 113 (2022).
[23] C. Eloy, N. Kofman, L. Schouveiler, The origin of hysteresis in the flag instability, J. Fluid Mech. 691 (2012) 583–593.
[24] S. Alben, M. Shelley, Flapping states of a flag in a inviscid fluid: bistability and the transition to chaos, Phys. Rev. E 100 (2008).
[25] Y. Kuznetsov, Elements of Applied Bifurcation Theory, Springer, 2004.
[26] M. Krack, J. Gross, Harmonic Balance For Nonlinear Vibration Problems, Springer, 2019.
[27] B. Cochelin, A path-following technique via an asymptotic numerical method, Comput. Struct. 53 (5) (1994) 1181–1192.
[28] L. Guillot, PhD Thesis, Marseille: Aix-Marseille Université, 2020.
[29] G. Hirs, A bulk-flow theory for turbulence in lubricant films, J. Lubr. Technol. 95 (1973) 137–146.
[30] J. Antunes, P. Piteau, A nonlinear analytical model for the squeeze-film dynamics of parallel plates subject to axial flow, J. Fluids Struct. 52 (2010) 1491–1504.
[31] R. Blevins, Fluid Dynamics, Van Nostrand Reinhold Company, New York, USA, 1984.
[32] F. Soares, J. Antunes, V. Debut, C. Vergez, B. Cochelin, F. Silva, A Galerkin formulation for the nonlinear analysis of a flexible beam in channel flow, J. Fluids Struct. (2023) pp. (pre-print).
[33] J.P. Boyd, The tau-method. Chebyshev and Fourier Spectral Methods, Dover Publications, New York, USA, 2000, pp. 473–479.
[34] E. Hairer, G. Wanner, Solving Ordinary Differential Equations II: Stiff and Differential-Algebraic Problems, Springer-Verlag, New York, 1996.
[35] "Manlab: an interactive path-following and bifurcation analysis software," [Online]. Available: http://manlab.lma.cnrs-mrs.fr/. [Accessed 23 November 2022].
[36] L. Guillot, B. Cochelin, C. Vergez, A generic and efficient Taylor series-based continuation method using a quadratic recast of smooth nonlinear systems, Int. J. 119 (5) (2019).
[37] L. Guillot, A. Lazarus, O. Thomas, C. Vergez, B. Cochelin, A purely frequency based Floquet-Hill formulation for the efficient stability computation of periodic solutions of ordinary differential equations, J. Comput. Phys. 416 (109477) (2020).
[38] R. Seydel, Practical Bifurcation and Stability Analysis: from Equilibrium to Chaos, Springer, New York, 1994.
[39] B. Cochelin, M. Medale, Power series analysis as a major breakthrough to improve the efficiency of asymptotic numerical method in the vicinity of bifurcations, J. Comput. Phys. 3 (2) (2013) 281–297.
[40] S. Karkar, B. Cochelin, C. Vergez, A high-order, purely frequency based harmonic balance formulation for continuation of periodic solutions: the case of non-polynomial nonlinearities, J. Sound Vib. 332 (4) (2013).
[41] G. Jankee, B. Ganapathisubramani, Influence of geometrical parameters on the hyteresis of flutter onset in confined configurations, Exp. Fluids 63 (2022).
[42] C. Eloy, R. Lagrange, C. Souilliez, L. Schouveiler, Aeroelastic instability of cantilevered flexible plates in uniform flow, J. Fluid Mech. 611 (2008) 97–106.
[43] C. Guo, M. Paidoussis, Stability of rectangular plates with free-edges in two-dimensional inviscid channel flow, J. Appl. Mech. 67 (2000) 171–176.
[44] T. Prasanth, V. Premchandran, S. Mittal, Hysteresis in vortex-induced vibrations: critical blockage and effect of m*, J. Fluid Mech. 671 (2011) 207–225.
[45] T. Colinot, PhD Thesis, Aix-Marseille Université, 2020.
[46] S. Michelin, S. Smith, B. Glover, Vortex shedding model of a flapping flag, J. Fluid Mech. 617 (2008) 1–10.
[47] M. Paidoussis, G. Li, F. Moon, Chaotic oscillations of the autonumous system of a constrained pipe conveying fluid, J. Sound Vib. 135 (1) (1989) 1–19.
[48] M.P. Paidoussis, G.X. Li, R.H. Rand, Chaotic motions of a constrained pipe conveying fluid: comparison between simulation, analysis, and experiment, J. Appl. Mech. 58 (1991) 559–565.